UNIVERSITY OF CALIFORNIA, SAN DIEGO

Devitrification Behavior and Interface Microstructure of Ni-based Amorphous Foils During Spark Plasma Sintering

A thesis submitted in partial satisfaction of the requirements
for the degree Master of Science

in

Materials Science and Engineering

by

Boyao Zhang

Committee in charge:

Professor Olivia A. Graeve, Chair
Professor Vitali Nesterenko
Professor Renkun Chen

2015

The thesis of Boyao Zhang is approved, and it is acceptable in quality and form for publication on microfilm and electronically:

Chair

University of California, San Diego

2015

TABLE OF CONTENTS

Signature Page iii

Table of Contents iv

List of Figures v

List of Tables viii

Abstract of the Thesis ix

1 Introduction 1

1.1 Spark Plasma Sintering (SPS) 1
1.1.1 Introduction of SPS 1
1.1.2 Mechanism of spark plasma sintering 5
1.2 Amorphous metal (metallic glass) 11
1.2.1 History of Amorphous Metal 11
1.2.2 Property of Amorphous Metal 15
1.2.3 Thermodynamic and kinetic behavior of amorphous metal 23

2 Experimental Methology 27

3 Result and Discussion 32

3.1 Thermodynamic characterization 32
3.2 X-ray diffraction patterns 36
3.3 Scanning electron microscopy (SEM) characterization 58

4 Summary 88

5 Reference 92

LIST OF FIGURES

Figure 1: Schematic spark plasma sintering (SPS) set up..……..3

Figure 2: Current distributions in the SPS die for alumina and copper samples. Applied voltage = 5 V……..9

Figure 3: Radial current density distribution for a non-conducting (alumina) and conducting (copper) samples. The profile is calculated along the diameter passing through the center of the sample. Applied voltage = 5 V…….10

Figure 4: A comparison of critical cooling rate and reduced glass transition temperature T_{rg} for BMG, silicate glasses and conventional metallic glasses……13

Figure 5: The picture of as-cast vitalloy BMG system ……14

Figure 6: Critical casting thickness for glass formation as a function of the year the corresponding alloy has been discovered……..15

Figure 7: The relations between mechanical properties of some typical BMGs……..16

Figure 8: Failure surface from a tensile sample which exhibited cup- and cone-type fracture. The droplets are indicating localized melting……..18

Figure 9: In situ images for crack tip branching in a single-edge notched tension sample during a fracture toughness experiment. The stress intensities at the main crack tip are shown below the images…….…18

Figure 10: Relationship between permeability and saturated magnetic flux density for Fe-based glassy alloys. The data of other soft magnetic alloys are also shown for comparison……..……...23

Figure 11: SPS experiment set up……..29

Figure 12: Free sintering experiment set up…….30

Figure 13: SPS samples after removing the graphite residual……..30

Figure 14: DSC curves of (a) Ni1, (b) Ni2, (c) Ni3, (d) Ni4, (e) Ni5, under three different heating rates. Legend is shown in right bottom corner……..……..33

Figure 15: Activation Energy of 5 Ni foils……..35

Figure 16: Ni1 XRD patterns obtained from SPS method..……...39

Figure 17: Ni1 XRD patterns obtained from pressureless sintering…….....40

Figure 18: Ni2 XRD patterns obtained from SPS method……..42

Figure 19: Ni2 XRD pattern under pressureless sintering method……43

Figure 20: XRD of the as-received Ni2 foils…..……44

Figure 21: Ni3 XRD pattern obtained from SPS method……..…..46

Figure 22: Ni3 XRD patterns obtained from pressureless sintering…… 47

Figure 23: Ni4 XRD patterns obtained from SPS method……..……50

Figure 24: Ni4 XRD patterns obtained from pressureless sintering……..51

Figure 25: Ni5 XRD patterns obtained from SPS method……..…….....54

Figure 26: Ni5 XRD patterns obtained from pressureless sintering……..55

Figure 27: Ni-based samples Full-Width-Half-Maximum (FWHM) map sintered by SPS and free sintering……58

Figure 28: SEM images of Ni 2 SPS sample sintered at T_x+10 K, and held for 20 min……..……..….60

Figure 29: (a) SEM images of Ni 2 SPS sample sintered at T_x+10 K, for 20 min, (b) and its corresponding EDX image……61

Figure 30: SEM images of Ni 2 SPS sample sintered at T_x+20 K, and held for 20 min…….63

Figure 32**:** SEM images of Ni 2 SPS sample sintered at T_x+50 K, and held for 20 min…….64

Figure 33: SEM images of Ni 2 SPS sample sintered at 873 K, and held for 20 min……...65

Figure 34: SEM images of Ni 3 SPS samples sintered at T_x+10 K, and held for 20 min…….67

Figure 35: SEM images of Ni 3 SPS samples sintered at T_x+20 K, and held for 20 min…….69

Figure 36: SEM images of Ni 3 SPS samples sintered at T_x+30 K, and held for 20 min……..……...71

Figure 37: SEM images of Ni 3 SPS samples sintered at T_x+50 K, and held for 20 min……..……...73

Figure 38: SEM images of Ni 3 SPS samples sintered at 873 K, and held for 20 min……..…….....75

Figure 39: SEM images of Ni 4 SPS sample sintered at T_x+10 K, and held for 20 min…….76

Figure 40: SEM images of Ni 4 SPS sample sintered at T_x+20 K, and held for 20 min…….79

Figure 41: Ni 4 SPS sample sintered at T_x+20 K, and held for 20 min: (a) SEM image; (b) corresponding EDX mapping; (c) and corresponding EDX spectrum ……81

Figure 42: Ni 4 SPS sample sintered at T_x+20 K, and held for 20 min: (a) SEM image; (b) corresponding EDX mapping; (c) and corresponding EDX spectrum ……82

Figure 43: SEM images of Ni 4 SPS sample sintered at T_x+30 K, and held for 20 min…….84

Figure 44: SEM images of Ni 4 SPS sample sintered at T_x+50 K, and held for 20 min…….87

Figure 45: SEM images of Ni 4 SPS sample sintered at 873 K, and held for 20 min……...89

LIST OF TABLES

Table 1: Sintering temperature of Ni-based samples……..30

Table 2: Slope and activation energy of five Ni-based foils……36

ABSTRACT OF THE THESIS

Devitrification Behavior and Interface Microstructure of Ni-based Amorphous Foils During Spark Plasma Sintering

by

Boyao Zhang

Master of Science in Material Science and Engineering

University of California, San Diego, 2015

Professor Olivia A. Graeve, Chair

We present a detailed study of the devitrification behavior of five Ni-based amorphous metal foils of different compositions, consolidated using spark plasma sintering (SPS) or pressureless sintering. Samples of approximately 1 mm thickness and 20 mm in diameter were prepared by stacking layers of amorphous foil on top of each other. The sintering temperatures were based on the crystallization temperatures (T_x) for each sample as determined from differential scanning calorimetry (DSC). Through detailed X-ray diffraction (XRD) analysis, full-width-half-maximum (FWHM) measurements and DSC analysis, we observed that the width of the 100% diffraction peak decreased

with increasing temperature. The changes in FWHM with temperature correspond to phase transformation process occurred at T_x+30 K, according to XRD phase identification. Microstructure analysis of the samples by scanning electron microscopy showed the current defects in SPS samples, which provide physical evidence of electric current effect during the SPS process. The formation of those unique morphologies was believed to relate to silicon atom, but more detailed analysis is still needed.

1 Introduction

1.1 Spark Plasma Sintering

1.1.1 Introduction to spark plasma sintering

By definition, sintering is the act of bonding particles/materials at high pressures and/or temperatures. It has been in use for more than 6000 years for making bricks and pottery and in the consolidation of precious metals in pre-Columbian South America.[1,2] One of the key points to achieve consolidation is the so-called “global” driving force. The global driving force for sintering is the reduction of Gibbs free energy (chemical potential or free enthalpy), usually associated with replacement of high-energy surfaces and grain boundaries with lower energy ones. Higher surface and grain boundary energies improve the likelihood of sintering to occur. The “local” driving force is the diffusion of atoms, which is calculated using the second derivative of the potential energy curve.[3] This process may take place at temperature below the melting temperature of the sintered materials (solid-state sintering) or at temperatures equal to or higher than the melting temperature of materials (liquid-phase sintering).

For economic reasons, significant efforts have been devoted to new methodologies to achieve higher density, lower activation energy and lower

sintering temperatures. Spark plasma sintering (SPS) is a process that has stimulated worldwide interest for the rapid consolidation of both powders and foils into bulk materials. Compared to conventional hot pressing techniques, lower sintering temperature, rapid heating rates (50-1000 K/min), and much shorter holding times are the most attractive features SPS has. Research on SPS has been completed on a wide variety of materials such as single phase metals, ceramics, composites,[4] nano-materials,[5] biomaterials,[6] intermetallics, and many other material systems.

The SPS process involves a consolidation of materials under a uniaxial pressure and action of electric current, as shown schematically in Figure 1. It is believed that electric current has contribution to consolidation process in SPS, making it fundamentally different form conventional hot pressing.[3] The use of electric current (or electric field) is not novel, but within the past few decades, significant efforts have been devoted to this field to understand the effect of electric field applied in this process. As studies have shown, an enhancement of sintering in the presence of an electric field is observed during the process.[7-16] A variety of materials have been tested in which SPS reaches higher densities and smaller grain sizes at lower temperatures and shorter holding times. However, the electric current seems to have different effects among different materials. When ceramic powders (non-conductive materials) are used, current only goes through the graphite die used during

the process, and contributes to the sintering process by internal Joule heating. For conductive materials, such as metallic powders and foils, the current has been shown to decrease the activation energy and enhance the kinetics, phase formation and mechanical properties of the resulting materials.

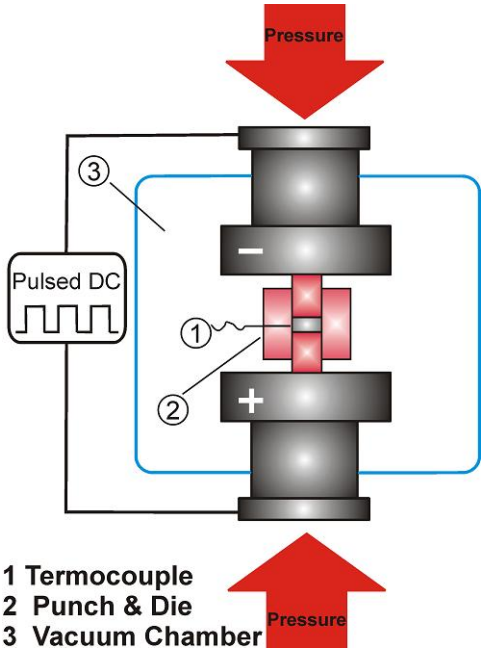

Figure 1: Schematic spark plasma sintering (SPS) set up.

Asoka-Kumar *et al.*[17] believed that the imposition of current is believed to improve the concentration of point defects (mainly vacancies) in metallic materials. They used in-situ positron annihilation spectroscopy (PAS) to demonstrate a marked increase in vacancy concentration under current imposition. In their research, $Bi_xSb_{2-x}Te_3$ compounds were used to evaluate the change of Hall mobility. It was found that the electric current induced atomic diffusion was responsible for a remarkable increase in Hall mobility and a moderate decrease in carrier density. In addition, they also found that

small grain size could be achieved and crystal defects could be modulated.

Garay *et al.*[12] proved that pulsed electric field could enhance the growth of intermetallic phases in the Ni-Ti system. They investigated the interface of the Ni-Ti system and identified the intermetallic compounds in the interlayer (NiTi, Ni_3Ti and $NiTi_2$) using multiple current densities. It was found that, with applied current, the growth rate of all product layers were significantly improved compared to current-free growth rates published earlier. In addition, the effective activation energy of all phases formed was found to decrease with increasing current density.

In Friedman' s work[11], Au-Zn diffusion couples were used to prove that high DC currents could strongly enhance the growth kinetics of phases they obtained from the interface area. In particular, AgZn, An_5Zn_8 and $AgZn_3$ intermetallic compounds were found. Compared to the current free experiment, the relative amount of AgZn was greatly increased. In addition, it was observed that the current effect was only observed after a threshold value.

Under the assumption that current plays a significant role in enhancing the consolidation kinetics and phase formation, a number of research projects have been completed to find out the possible effects of electric current direction, pulsed frequency and wave shape. Zhao[18] has used Cu-Ni-Cu sandwich-structure foil interdiffusion couples sintered under SPS to

explore the direction effect of electric field (current). The interdiffusivity showed an obvious increase as the current density increased when electronic flow was from Ni to Cu (co-current interface). However, the interdiffusivity of Cu to Ni interface stayed constant as the current density increased.

Besides enhancement in thermodynamics, the current also influences the kinetics in metallic systems. This enhancement effect is believed to relate to an electron wind effect, which indicates that the role of current is more complex. Garay *et al.*[13] used positron annihilation spectroscopy (PAS) and successfully proved the stability of metastable defects in Ni_3Ti was reduced under applied high current. In addition, the research also found that the activation energy was reduced under the influence of current, which indicates that more diffusion events became activated with the application of a current.

1.1.2 Mechanisms of spark plasma sintering

While a large amount of research and a wide range of materials have been studied using SPS, there are insufficient mechanistic descriptions of the process in metal or ceramic systems. Historically, this technique has been called spark plasma sintering because the existence of plasma was used to explain the enhancement effect of SPS.[19] However, there is still no direct and convincing paper reporting that plasma or spark exists during the

sintering process. Hulbert *et al.*[2] have set up a complex experiment using electrical and optical techniques to investigate the process occuring inside the SPS. The experiment did not produce evidence for the presence of plasma, which is not surprising. The situations in SPS are not complex enough for plasma to generate and stabilize.

However, the presence of strong electric fields together with thermal and pressure gradient could generate a relatively complex environment, where several basic processes can affect the materials at the same time. Theoretically, in a vacuum experiment environment with application of strong electric field, three classes of discharge should be taken into consideration: arcs, sparks, and glow discharges.[20] Each requires certain conditions to occur, according to different gas pressure, applied voltage, discharge current, morphology and chemical properties of the surfaces. The spark discharge is used for discontinuous processes, with high current (usually kA range), and high voltage pulses (kV range).[21] The arc discharge often occurs under continuous processes applied with high discharge current (typically 10A or greater) and low voltage (tens of Volts).[22] In addition, the glow discharges require relatively low currents, 1 A or less, and with relatively high excitation voltages (300V or more).[23] Due to these requirements, arc discharge would be the most likely discharge process occurring during SPS.

Besides arc and spark discharge, electromigration is another theory

which attracts much attention. It is a mass transport phenomenon mainly observed in metals, associated with the momentum transfer between the conducting electrons and the metal ions. Consequently, electromigration may produce a migration of materials under high intensity of electronic flux. However, this momentum transfer requires current above 1000 A/cm^2.

The definition of electromigration relates to correlation between moving components under the external driving force. The theory and model of electromigration has been studied for years. Many models have been established, from the classical ballistic models to the latest quantum-mechanical approaches.[24,25] However, the experimental observation of this phenomenon is still lacking. Under the assumption of irreversible thermodynamics, the motion of an *i*th component depends on its interaction with all the other components. Atomic flux, J_i, is described by:

$$J_i = \sum_J L_{ij} X_j \ (i = 1,2, \dots, n)$$

In a pure metal, the flux of atoms could be rewritten as:

$$J_a^E = \frac{D_a c}{kT} Z^* eE = \frac{D_a c}{kT} Z^* e\rho j$$

Where D_a is the atomic diffusivity, c the vacancy concentration, k the Boltzmann's constant, T the absolute temperature, e the electronic charge, E the applied electric field, and j the current density. Z* is called the effective charge of the atom and is generally considered to be composed of two

elements:

$$Z^* = Z_{el}^* + Z_{wd}^*$$

Where Z_{el}^* is the nominal valence of the metal ion; while Z_{wd}^* represents for the momentum exchange between the carriers and the metal ions. The term $Z_{wd}^* eE$ is generally referred to as the “electron wind force”. Under the assumption that metals are lack of the direct electrostatic component, the electron wind term usually dominates. According to the equations, the magnitude of electron wind depends on the natural material properties.

In experiments, electromigration will be strongly affected by temperature and microstructure of the sample. In the SPS experiment, high sintering temperature will enhance the electromigration significantly. Mass transfer induced by eletromigration is very sensitive to the microstructure and the particular material. However, in a solid-sate reaction situation, the contribution of electromigration to the overall atomic flux and growth of the interfacial product has a close relationship to the relative values of the effective charge and of the intrinsic diffusivity of each kind of atom. There are four typical situations evaluated in Hsu’s paper.[26]

One may conclude that the electromigration contribution to the overall mass transfer is limited. In the SPS process, it is important to consider the intense current flow; several thousand amps may be utilized in the experiment. However, according to the modeling work done by

Anselmi-Tamburini, only a fraction of current can flow through the sample, even if the sample is highly conductive.[17] The fraction of total current flowing through the sample, shown in Figure 2 and Figure 3, varies with sample thickness and conductivity. In the case of a highly conductive metal, 3mm thick samples would have accommodated 60% of the total current flow. This argument would suggest that electromigration in SPS may have been overestimated in previous research.

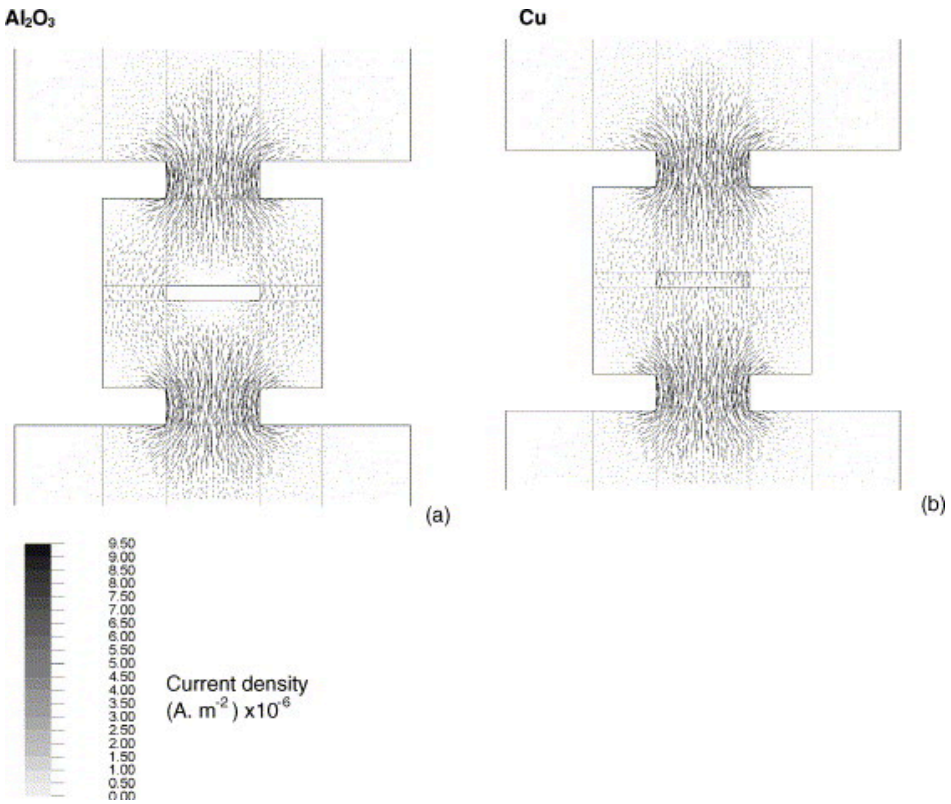

Figure 2: Current distributions in the SPS die for alumina and copper samples. Applied voltage = 5 V.[17]

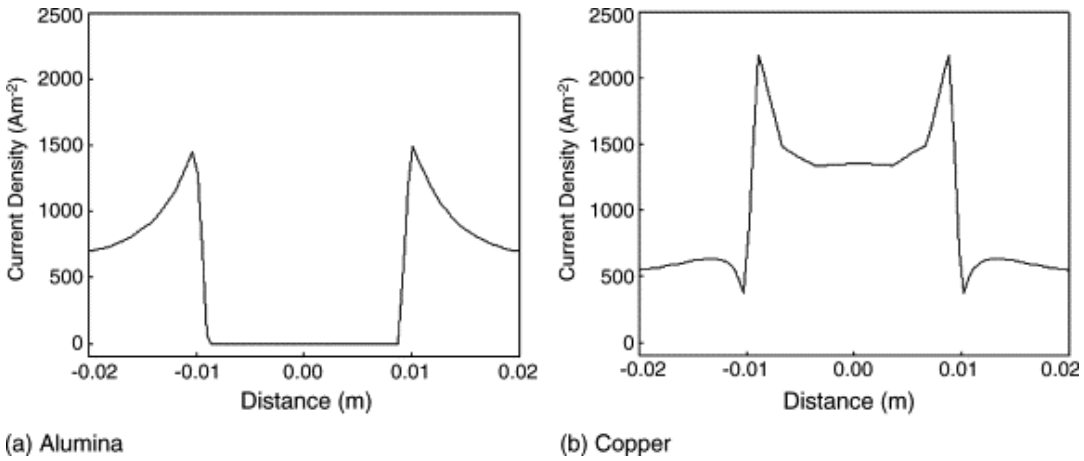

Figure 3: Radial current density distribution for a non-conducting (alumina) and conducting (copper) samples. The profile is calculated along the diameter passing through the center of the sample. Applied voltage = 5 V.[17]

To evaluate the current flow issue during SPS process, Frei *et al.*[10] has modified the experiment, using a classical metal sphere on plate inside the SPS apparatus to force all the current to flow through the sample. With this experimental design, the current density effect on metallic system (copper) has been investigated well. It was reported that increasing current density utilized in SPS would enhance the phase formation kinetics. Similar work has also been studied using a tungsten sphere and plate.[15] In addition, planar diffusion couple geometry has also been used to evaluate the current effect in mass transport.

In metallic systems, a thin oxide layer covering the surface should also be taken into consideration, because oxide materials often have dielectric properties. According to the calculations from Techaumant and Takuma,[27] externally applied electric field would generate a high local electric field in the vicinity of the oxidation layer during the early sintering stage. Though the

oxidation layer in metallic sintering systems should be thin, the significant local electric field induced polarization effects would have relevant influence on the beginning of the sintering process. This issue has been evaluated in powder systems, and deserves more attention.

Reviewing the previous work, current effect on thermodynamics and kinetics have been discussed without a convincing conclusion. However, there is little work focusing on amorphous materials, especially bulk metallic glasses. In addition, there is no direct report of observation of current effect on materials sintering behavior.

1.2 Amorphous metals (metallic glasses)

1.2.1 History of Amorphous Metals

Amorphous metals, also known as metallic glasses, have received considerable attention because they present unique mechanical and magnetic properties. By definition, a metallic glass or amorphous metal, is a solid metallic material, usually an alloy, with a disordered atomic-scale structure. Amorphous metals have a glass-like atomic structure, are electrically conductive, and have good thermal conductivity. Duwez and his coworkers discovered the first metallic glass by rapid quenching, at 10^5-10^6 K/s, and obtained a $Au_{75}Si_{25}$ alloy[28]. Duwez's work has attracted increasing attention because of its fundamental scientific importance. Amorphous

metals are the newest addition to the solid-sate amorphous materials family.

Turnbull *et al.*[29] have illustrated the similarities between metallic glasses and other non-metallic glasses. They reported that a glass transition manifested in conventional glass-forming melts could also be observed in rapid quenched metallic glasses. They even defined reduced glass transition temperature $T_{rg}= T_g/T_m$, where T_g is the glass transition temperature, and T_m is the melting point. T_{rg} could be used to determine the glass-forming ability (GFA) of an alloy. According to Turnbull's criterion, a liquid with $T_g/T_m = 2/3$ can only crystallize within a narrow temperature range, and suppression of crystallization may occur at a relatively low cooling rate. Turnbull's criterion is a rule of thumb predicting the GFA of any liquid. In empirical rules, Inoue has summarized three criteria for multicomponent alloys glass formation:[30] (1) multicomponent system consisting of more that three elements; (2) significant difference in atomic sizes with the size ratio about 12% among the three main constituent elements; and (3) negative heats of mixing among the three main constituent elements.

For engineering applications, bulk metallic glasses (BMG) are required. "Bulk", arbitrarily defined as the millimeter scale in Wang's[31] review paper, was first produced using the suction-casting method by Chen in 1974. The critical cooling rate for BMG formation by Chen was 10^3 K/s, which was 3 orders of magnitude lower than conventional metallic glasses. However, the

Pd-based alloy Chen used to produce BMGs, is costly and prohibited further development. In the late 1980s, Inoue investigated rare-earth materials with Al and Fe-based metals. These multicomponent metallic glass systems require even lower critical cooling rates and have better glass-forming ability, as shown in Figure 4. La-Al-Ni and La-Al-Cu had exceptional GFA.[32] Later, they replaced Fe and Ni with alkaline-earth metal Mg, creating Mg-Cu-Y and Mg-Ni-Y,[33] as well as with the Zr-based BMG family. The manufacturing method consisted of casting the alloy melt in water-cooling Cu molds to obtain fully glassy rods and bars, with sizes of up to several millimeters.

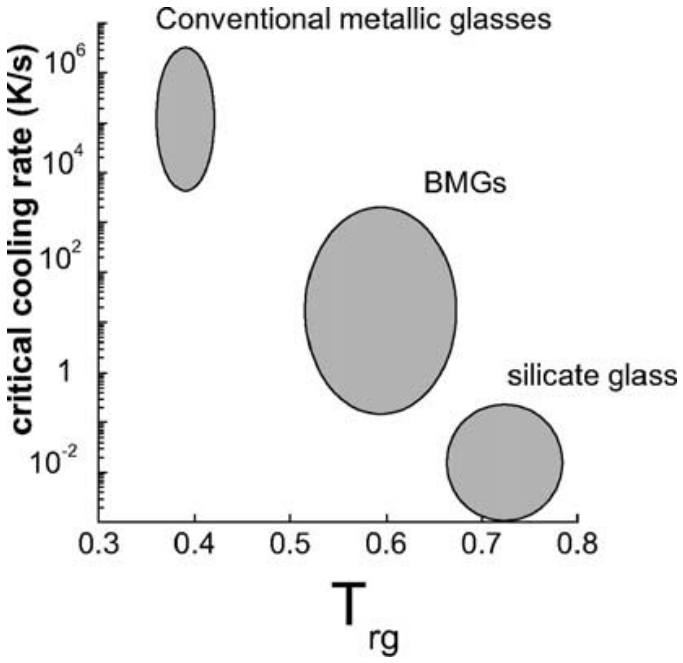

Figure 4: A comparison of critical cooling rate and reduced glass transition temperature T_{rg} for BMG, silicate glasses and conventional metallic glasses.[31]

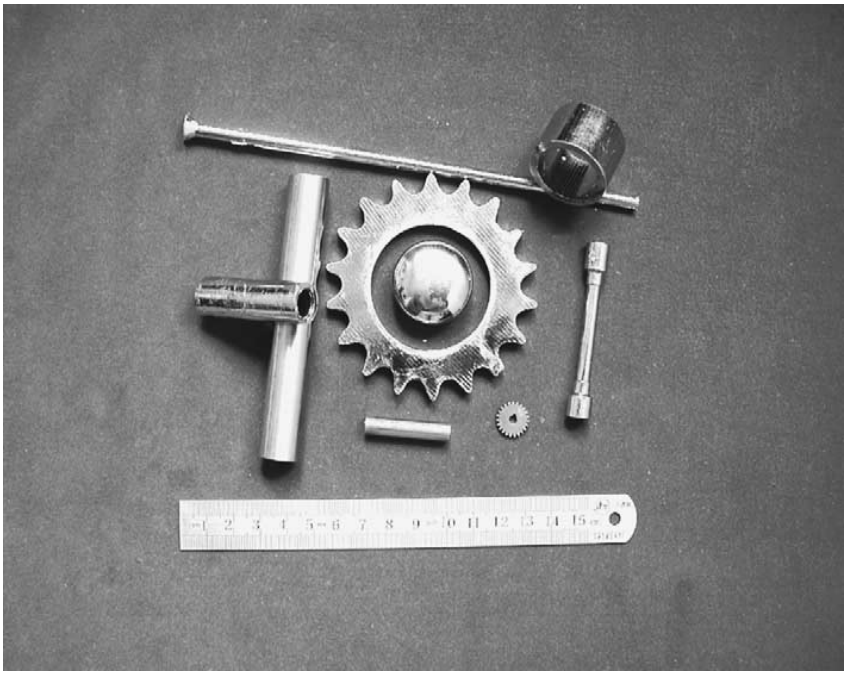

Figure 5: The picture of as-cast vitalloy BMG system.[31]

Peker and Johnson[34] in Caltech developed the quinary alloy $Zr_{41.2}Ti_{13.8}Cu_{12.5}Ni_{10}Be_{22.5}$, commonly referred to as Vitreloy 1 (Vit1). Vit1 has been the subject of Department of Energy and NASA research of aerospace materials. A high quench rate is used to obtain this metallic glass, with critical diameter up to several centimeters. It is clear that metallic glass has potential for engineering applications. Figure 6 shows the critical casting thickness as a function of the year in which the corresponding alloy was developed. The critical thickness has increased by more than three orders of magnitude in the last 40 years. The linear fit represents a thickness increase by one order of magnitude every 10 years.

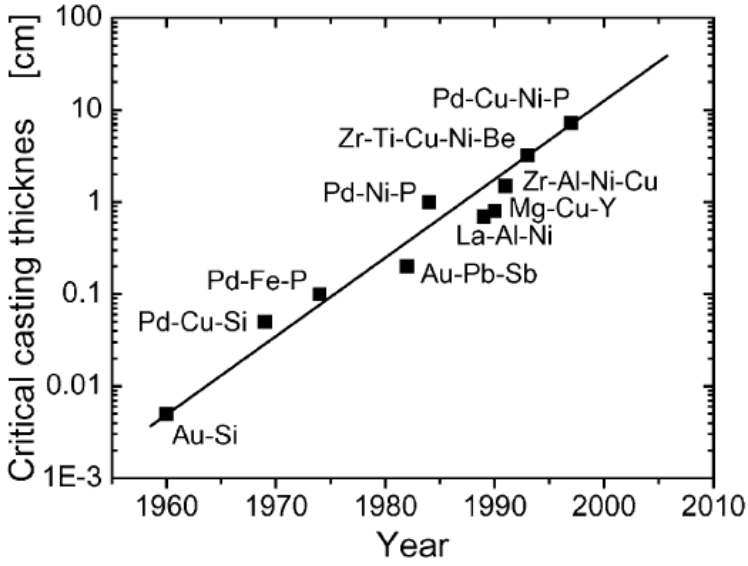

Figure 6: Critical casting thickness for glass formation as a function of the year the corresponding alloy was discovered.[35]

Besides rapid quenching casting, a variety of amorphization techniques were developed in the 1980s, including physical vapor deposition, solid-state reaction, ion irradiation and mechanical alloying. Those techniques employ totally different mechanisms with respect to the conventional rapid quenching technique.

1.2.2 Properties of Amorphous Metals

1.2.2.1 Mechanical Properties of Amorphous Metal

In the past decades, amorphous metals, especially BMGs, have attracted much attention from researchers, because of their unique atomic structure and many excellent physical and chemical properties. These properties

give BMGs promising potential for engineering applications.

Figure 7 illustrates the relationship between tensile fracture strength ($\sigma_{t,f}$),Young's modulus (E), and Vickers hardness (H_v) for typical BMGs. Tensile strength and Vickers hardness have a roughly linear relationship to Young's modulus. Besides BMGs, conventional crystalline alloy data points were also included in the figure, which show a steeper slope, compared to BMGs, and indicate the high elastic limits of the BMGs. BMG data points are more linear than conventional crystalline alloys, because BMGs have an ideally homogenized solid solution over the whole range of compositions.

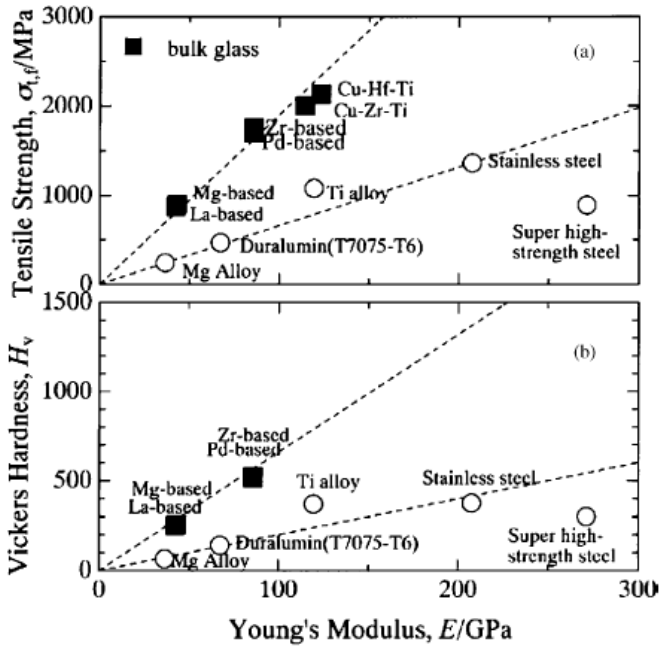

Figure 7: The relationships between mechanical properties of some typical BMGs: (a) tensile fracture strength ($\sigma_{t,f}$) with Young's modulus (E); (b) Vickers hardness (H_v) with Young's modulus (E).[36]

BMGs have higher tensile strength and lower Young's moduli compared

to typical crystalline alloys. This difference between amorphous metals and crystalline metals is considered a result of different deformation and fracture mechanisms. In metallic glasses, the deformation is usually related to inhomogeneous flow in highly localized shear bands. In Figure 8, the sample was under tensile strain. The morphology of its fracture surface indicates that, under a high strain rate, unstable fracture occurs associated with an associated local melting phenomenon. Due to the highly localized nature of flow in metallic glasses, shear band formation typically leads to catastrophic failure. It is believed that the localization of shear is associated with possible strain-softening mechanisms and thermal softening as well as the absence of strain-hardening (work hardening) mechanisms. For fracture toughness measurement, Katharine[37] used single-edge notched tension samples for modifying the plastic strain field at the crack tip, as shown in Figure 9. As described in their report, the damage zone is well constrained in the classical plastic zone. To confirm the experimental results, they developed a model within Zr-Ti-Ni-Cu-Be system to evaluate the deformation mechanism in metallic glass. In the model, they resolved surface temperature increase and subsequent dissipation associated with crack tip plasticity in BMGs. The resulting maximum temperatures were in agreement with a nonhardening plasticity model for the heat generated by a propagating crack. From this report, adiabatic heating, which occurs during

the localized shear bands has been confirmed.

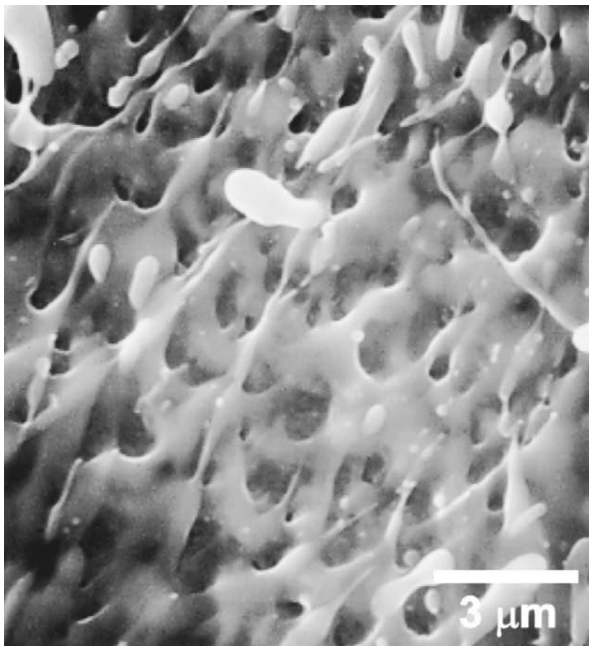

Figure 8: Failure surface from a tensile sample which exhibited cup- and cone-type fracture. The droplets are indicating localized melting.[35]

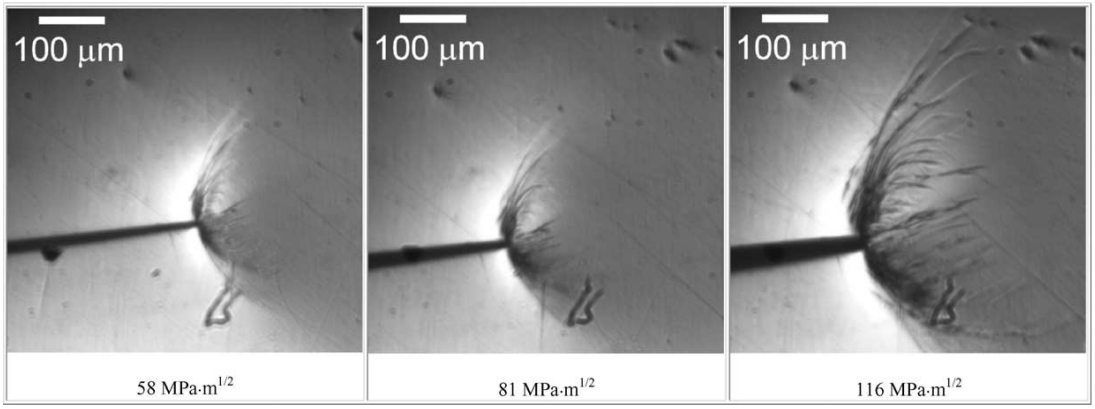

Figure 9: In situ images for crack tip branching in a single-edge notched tension sample during a fracture toughness experiment. The stress intensities at the main crack tip are shown below the images.[38]

As one of the most promising BMGs, Vit1, which is a Zr-Ti-Ni-Cu-Be alloy system, has had its mechanical properties studied in detail.[37,39] It was found that Vit1 exhibits high Charpy impact fracture energies of approximately 110

to 140 kJ/m^2 and high fracture toughness.[30] However, its fatigue limit is nearly the same as conventional crystalline alloys. Useful crystalline metals have continuous plastic strain followed with yielding, and these properties will give them high fracture toughness and impact resistance. In contrast with crystalline metals, metallic glasses are usually brittle, namely there is no plasticity presented. Johnson's group[39-42] has done a variety of work exploring the mechanical properties of Vitreloy, especially Vit1 ($Zr_{41.2}Ti_{13.8}Cu_{12.5}Ni_{10}Be_{22.5}$), in particular fracture toughness and fatigue-crack propagation have been tested. It has been determined that the alloy exhibited fracture toughness values of K_{Ic} ~ 55 MPa/m^2, which was comparable with high-strength steel or aluminum alloys.[39] However, when there is crystallization occurring in the material, even if it is partially crystalline, a drastic deduction in fracture toughness is observed. During a test of fatigue-crack propagation, it was also found that crystallization increases the fatigue-crack propagation rate dramatically. These results indicate the fact that Vit1 still can have improved performance for engineering applications, in particular, for long-term uses. As a result, researchers have modified the composition by adding new elements,[43] using reinforced metallic fiber,[44] or a ductile phase[41] to improve mechanical properties.

Besides the Viteloy series, other series of metallic glasses have been developed and improved using similar methodologies. By adjusting the

microstructure of metallic glasses, a better understanding and evaluation of deformation mechanisms and glass structures could be studied. There are several important points for improving mechanical properties that have been mentioned in Schuh's[45] review paper, including understanding shear band formation, fracture length scale, and deeper connections to glass structure.

1.2.2.2 Magnetic Properties of Amorphous Metals

For BMGs that contain Fe, magnetic properties have attracted much attention, both hard magnetic and soft magnetic properties.

In a Nd(Pr)-Fe based system, its high coercivity and the absence of glass transition before crystallization in isochronal DSC experiments have made it one of the most promising candidates for engineering applications.[46] According to several research papers, it is believed that the homogeneous disordered atomic structure is responsible for the exceptional coercivity. Several researchers have made efforts to evaluate the relation between its atomic structure and magnetic properties.[47] Xing and coworkers studied Nd-Fe-B-Co-Al BMG obtained from copper mold casting and melt spinning under different cooling rates.[47] Both of them were amorphous according to XRD detection, but the casting cylinders showed hard magnetic while the spinning ribbon showed soft magnetic properties. They considered that the

casting cylinders obtained from a slower cooling rate might contain metastable ordered clusters, which would contribute to the much larger coercivity than ribbon samples. In addition, Wei *et.al.*[48] have also annealed this kind of BMG at 715 K and reported that the short-scale ordered atomic clusters have domain among the material. This resulted in a stronger transition coupling, which is considered to have close relationship to higher transition-metal concentration in the amorphous phase due to the precipitation of Nd crystalline phase. The interesting part of this report is that both the casting cylinder and spinning ribbon showed no crystallization peak along the whole range of DSC tests. In addition, there are also papers reporting that heavy rare earth element-rich amorphous metals did not show hard magnetic properties at room temperature. As a result, the mechanisms for hard magnetic properties of BMGs and the relation between their microstructure and magnetic properties are still unclear.

Besides hard magnetic properties, Fe-based and Co-based BMGs often present ferromagnetism at room temperature. They have been developed from mold casting or water quenching since 1995.[49] Since then, those multicomponent materials have received increasing attention because of easy access of Fe and Co as well as industrial application potential. There are several main types of Fe-based and Co-based BMGs, including Fe-(Al, Ga)-(P, C, B, Si, Ge), Fe-TM (TM = IV-VIII group transition metal), and

Co-Fe-(Zr, Hf, Nb)-B. They are soft magnetic BMGs and the effective ways to improve the GFA as for other BMGs works well for Fe-based and Co-based BMGs. In addition, it has been reported that additional metalloid element Si could extend the saturation magnetization and reduce the coercive force. As mentioned in Shen's paper,[50] the addition of Si and Mo into a Fe-Ga-P-C system resulted in four amorphous alloy rods obtained from mold casting, with high saturation magnetization. They found out that simultaneously adding Si and Mo could effectively extend the supercooled liquid region and constrain the precipitation of the primary crystalline phase. This might contribute to better GFA and good soft magnetic properties.

As mentioned in Inoue's review paper,[51] Fe-based and Co-based BMGs have high electrical resistivity, higher initial permeability and better high frequency permeability compared to ribbon samples. However, the high materials cost and lower saturated magnetic flux (Figure 10) might be the main obstacles for its further development into industrial applications.

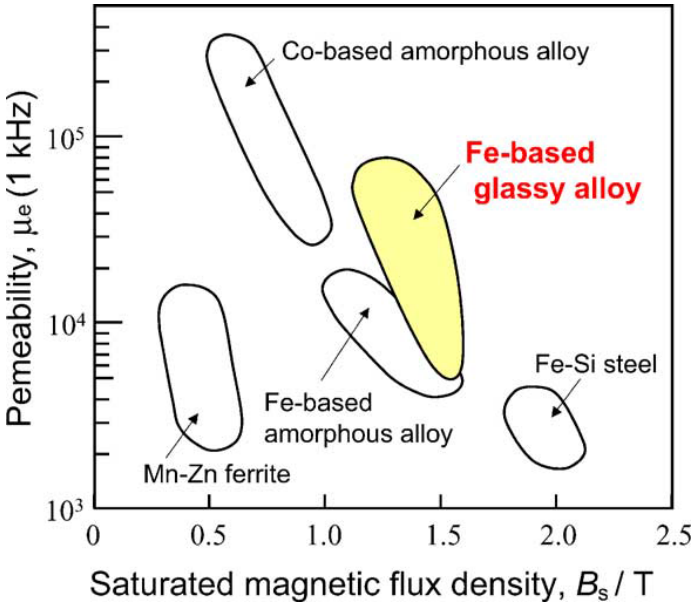

Figure 10: Relationship between permeability and saturated magnetic flux density for Fe-based glassy alloys. The data of other soft magnetic alloys are also shown for comparison.[49]

1.2.3 Thermodynamic and kinetic behavior of amorphous metals

Thermodynamically, bulk metallic glasses exhibit a low driving force for crystallization in the supercooled region. This low driving force will result in low nucleation rate and therefore improved GFA. Usually, thermal analysis is used to determine the Gibbs free-energy difference ΔG_{l-s} between the supercooled liquid and crystalline solid. Apparently, a small difference will contribute to high GFA, which could be calculated mathematically. As a supercooled liquid, metallic glass stays metastable at room temperature and has high viscosity and sluggish kinetics. Under DSC thermal analysis trace, it exhibits multiple exothermic reactions, corresponding to different degrees of microstructure relaxation and crystallization. As a result, metallic glasses

experience a glass transition at T_g and start to nucleate as temperature increases beyond crystallization temperature (T_x). Consequently, there is much space to explore the behavior of nucleation and crystallization. Those results have significant meaning for deeper understanding of the glass-forming ability and thermal stability of metallic glass, and production of nanocrystalline composites from controlled crystallization.

Due to pre-existing nuclei in metallic glass, it is common to obtain large density of nuclei and sluggish growth kinetics during the experiment. Generally, DSC has been widely used to investigate the crystallization kinetics, for the reason that heating rate, target temperature and heating environment could be precisely controlled while the mass difference and thermal information could be measured in detail.

As one of the most promising bulk metallic glasses materials, there has been much research conducted on the Vitalloy system. Shchroers and his group[52-55] have designed a series of experiments to investigate the crystallization kinetics of Vitalloy. Repeated annealing at different temperatures associated with the supercooled region has been studied.[54] The material is Vit1, and the annealing temperatures are 907, 860, and 750 K. According to the onset of crystallization time of each cycle, they found out that at high temperatures, the crystallization was governed by the time scale of the statistical nucleation events. At low temperatures, the crystallization

is controlled by diffusion, resulting in a well-defined onset time for crystallization. In addition, the heating rate effect to crystallization kinetics in Vit1 system was also explored.[56] The same group used a different heating rate and the same cooling rate to evaluate the onset time of crystallization. They reported that the crystallization process was highly history dependent, and they considered accumulation process and subsequent nuclei growth might contribute to this phenomenon.

Other researchers have also evaluated other factors that might have an effect on metallic glass crystallization including pressure,[57,58] annealing time[59] and electric current assistance.[16,60] Wang *et al.*[57] have used Vitalloy under various pressures and temperatures. They obtained composites with fine nanocrystalline structure in an amorphous matrix. It is believed that the high pressures have avoided the free volume and reduced voids through compressing the glassy structure and reconstructing the atomic configuration. On the other hand, metallic glasses have low atomic mobility and a highly dense microstructure, which will slow down the atomic rearrangement in a long range. However, with DC current, metallic glasses tend to have lower thermal stability according to Holland's report.[60] In their work, Vit1A and PCNP were used to evaluate the current effect on crystallization kinetics. Compared with annealing samples without current assistance, both the crystallites size and volume have increased. In the discussion part, a

current induced enhancement effect has been viewed as the main reason for this. It is believed that current has a positive effect on atomic diffusion and increases the free volume in a glassy structure.

2 Experimental Methodology

There are five kinds of Ni-based amorphous metal foils used in these experiments. The compositions of these five foils were $Ni_{40}Fe_{40}Si+B_{19}Mo_{1+2}$ (Ni1), $Ni_{78}B_{14}Si_8$ (Ni2), $Ni_{75.47}Cr_{19}Si_{4.5}Fe_{4.2}B_{2.8}C_{0.03}$ (Ni3), $Ni_{72.12}Cr_{19}Si_{7.3}B_{1.5}C_{0.08}$ (Ni4) and $Ni_{88.9}P_{11}C_{0.1}$ (Ni5). Ni1 and Ni2 were purchased from Goodfellow Inc., and Ni3 through Ni5 were purchased from Metglas. The size of Ni1 and Ni2 were 30 mm in width, and 25 μm in thickness. For Ni3 through Ni5, the width was 50mm, and the thickness was approximately 30 μm.

Before sintering, differential scanning calorimetry (TA instrument SDT Q600 TGA-DSC) was used to determine the glass transition temperature (T_g) , onset temperature of crystallization (T_{ox}) and crystallization temperature (T_x) of all foils. Seven different heating rates were used to measure the heat flow, from 5 K/min, 10 K/min, 15 K/min, 20 K/min, 25 K/min, 30 K/min, to 100K/min. The testing temperature range was from room temperature (about 500 K) to 1073 K. According to previous DSC trace analysis, amorphous metal usually presents multiple crystallization stages after T_g and corresponding T_{ox}.[61] Each heating rate has been repeated five times for consistency. The approximate amount of sample used for DSC analysis was 12 mg and a platinum crucible was used due to its higher thermal

conductivity. From DSC, the heat flow curve was obtained directly, but glass transition temperatures (T_g) were obtained by first derivation of the heat flow curve, picking up the changing temperature from negative to positive. The crystallization temperature (T_x) was obtained by second derivative analysis of the heat flow curve.

Foils were cut into a circle shape by scissors manually, with diameter 18.75 mm, with respect to the inner diameter of the spark plasma sintering (SPS) graphite die. The SPS experiment was done using a HD D 10 spark plasma sintering furnace (FCT Systeme GmbH) with 18.75 mm inner diameter graphite dies lined with graphite paper. As shown in Figure 11, 35-40 pieces of foils were stacked while SPS was conducted resulting in approximately 1mm thick disks. The applied load was 27 kN and the SPS sintering cycle specified reached the sintering temperature in an argon atmosphere. After the load was released, the sample was left for cooling down by turning the system off. In addition, a free sintering experiment was carried out in a box furnace (Thermo Lindberg Blue), covered by alumina plates both on the bottom and top, as shown in Figure 12. Two steel plates were loaded on the top to supply uniform pressure. The pressure for free sintering is less than 1 MPa. Both SPS and free sintering experiments were done at the same temperatures and heating rate, but the dwell holding time was different due to a tremendous pressure difference between those two

methods. The holding time for SPS was 20 min, and free sintering was 2 h. The sintering temperatures were as follows.

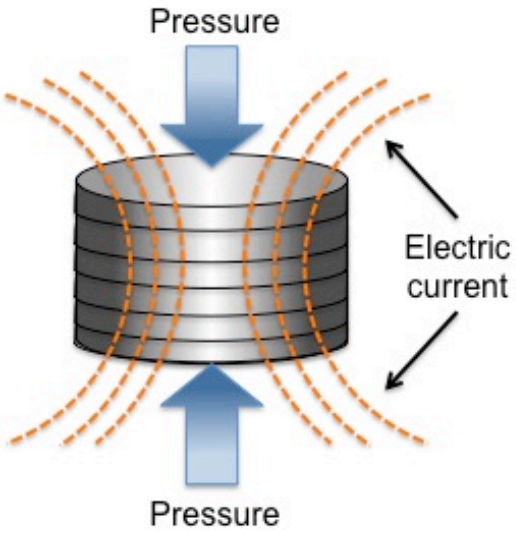

Figure 11: SPS experiment set up

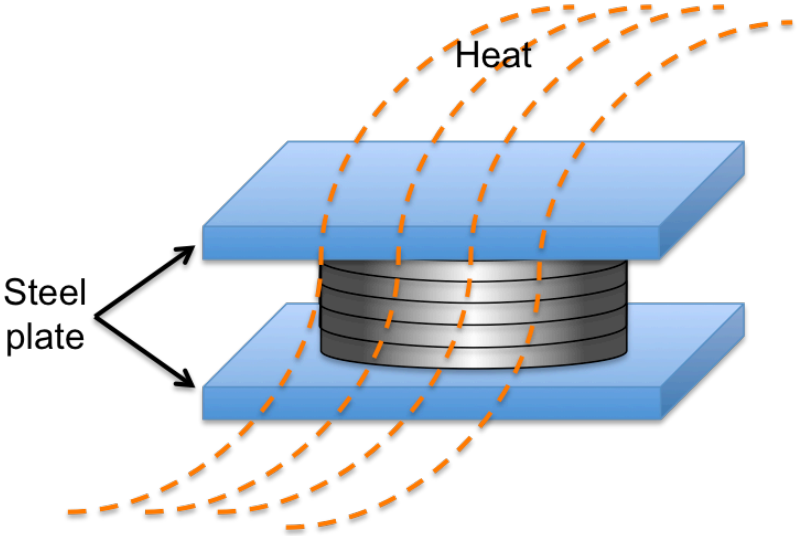

Figure 12: Free sintering experiment set up

Table 1: Sintering temperature of Ni-based samples

Temperature (K)	T_x+10	T_x+20	T_x+30	T_x+50	873 K (600 °C)
$Ni_{40}Fe_{40}Si+B_{19}Mo_{1+2}$	749	759	769	789	873
$Ni_{78}B_{14}Si_8$	776	786	796	816	873
$Ni_{75.47}Cr_{19}Si_{4.5}Fe_{4.2}B_{2.8}C_{0.03}$	749	759	769	789	873
$Ni_{72.12}Cr_{19}Si_{7.3}B_{1.5}C_{0.08}$	763	773	783	803	873
$Ni_{88.9}P_{11}C_{0.1}$	770	780	790	810	873

After SPS, every sample was polished to remove the residual graphite, as shown in Figure 13. To analyze their phase formation and crystallinity, each sample was characterized using a Bruker® D2 Phaser X-ray diffractometer (XRD). During XRD, samples were put on a zero-background sample holder under Cu $K\alpha$ radiation. Scans were conducted over a 2θ range from 30° to 85° using a step size of 0.04° and a dwell time of 1 s. DiffracEva® was used to analyze the phases present in each sample and calculate the Full-Width-Half-Maximum (FWHM) of the primary peaks.

Figure 13: SPS sample after removing the graphite residual.

To explore the microstructure and bonding mechanisms, samples were imaged using a scanning electron microscope (SEM). Interfaces of each sample were observed thoroughly under different magnifications. For SEM sample preparation, each specimen was held by a sample spacer perpendicularly in order to have its intersection exposed for polishing. Both placer and samples were embedded in epoxy, and then subsequently polished by abrasive disc and diamond suspension. SiC grinding papers were used for rough polishing (XP8 TedPella Inc.) and oil-based diamond suspension (Advance Abrasive) was used for fine polishing. Finished with a flat and scratch-free surface, samples were analyzed by a Philips XL30 field emission environmental scanning electron microscope (ESEM) at a voltage of 10 kV.

3 Result and Discussion

3.1 Thermodynamic characterization

In the DSC experiment, several heating rates were used. DSC curves under 5, 15, and 30K/min were plotted in Figure 14. The heat flow curves possessed higher intensity as heating rate increased. As shown in Figure 14(a)-(e), multiple exothermic events were observed in the five Ni-based amorphous foils along the experimental temperature range. The temperatures with the maximum heat flow of each exothermic event were labeled T_{xi}, although what those peaks represent is still unclear. The onset temperature of the exothermic event was labeled T_{oxi}. The multiple exothermic events indicated that there were several crystallization stages occurring throughout the sintering process. T_{oxi} was the starting point of each exothermic crystallization stage.

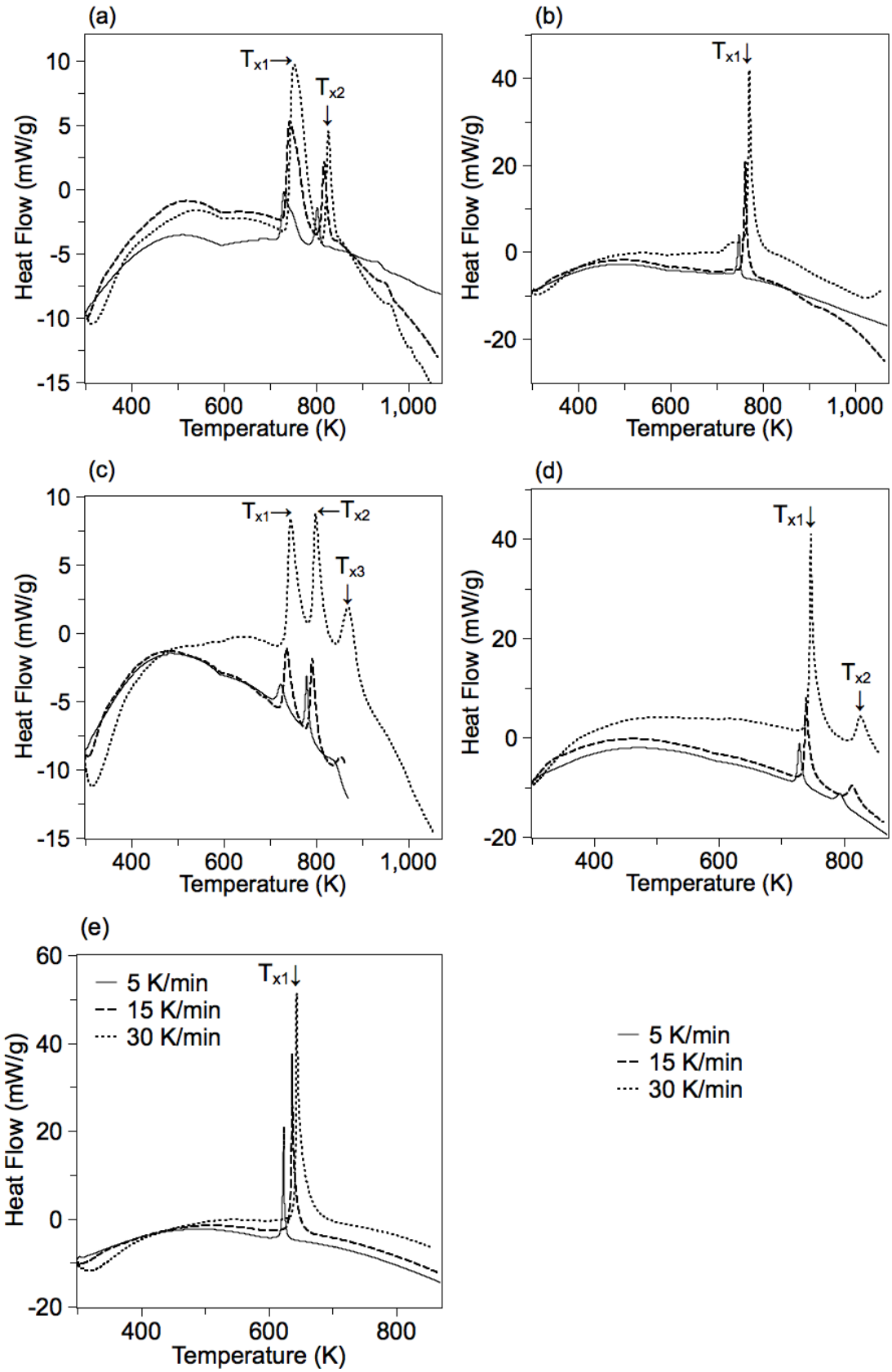

Figure 14: DSC curves of (a) Ni1, (b) Ni2, (c) Ni3, (d) Ni4, (e) Ni5, under three different heating rates. Legend is shown in right bottom corner.

According to the Kissinger method,[62] described in Equation 1, activation energy of the non-isothermal reaction could be calculated by T_{xi} under a different heating rate.

$$ln(\frac{\emptyset}{T_x^2}) = -\frac{E_a}{RT_x} \quad \text{Equation 1}$$

Figure 15 is a series of plots of activation energies determined by the Kissinger method for five Ni-based amorphous foils. The correlation coefficients were close to 1, indicating excellent linear fits. The slopes and the corresponding activation energies were presented as follows. The activation energies of each exothermic reaction and their corresponding slopes were shown in Table 2.

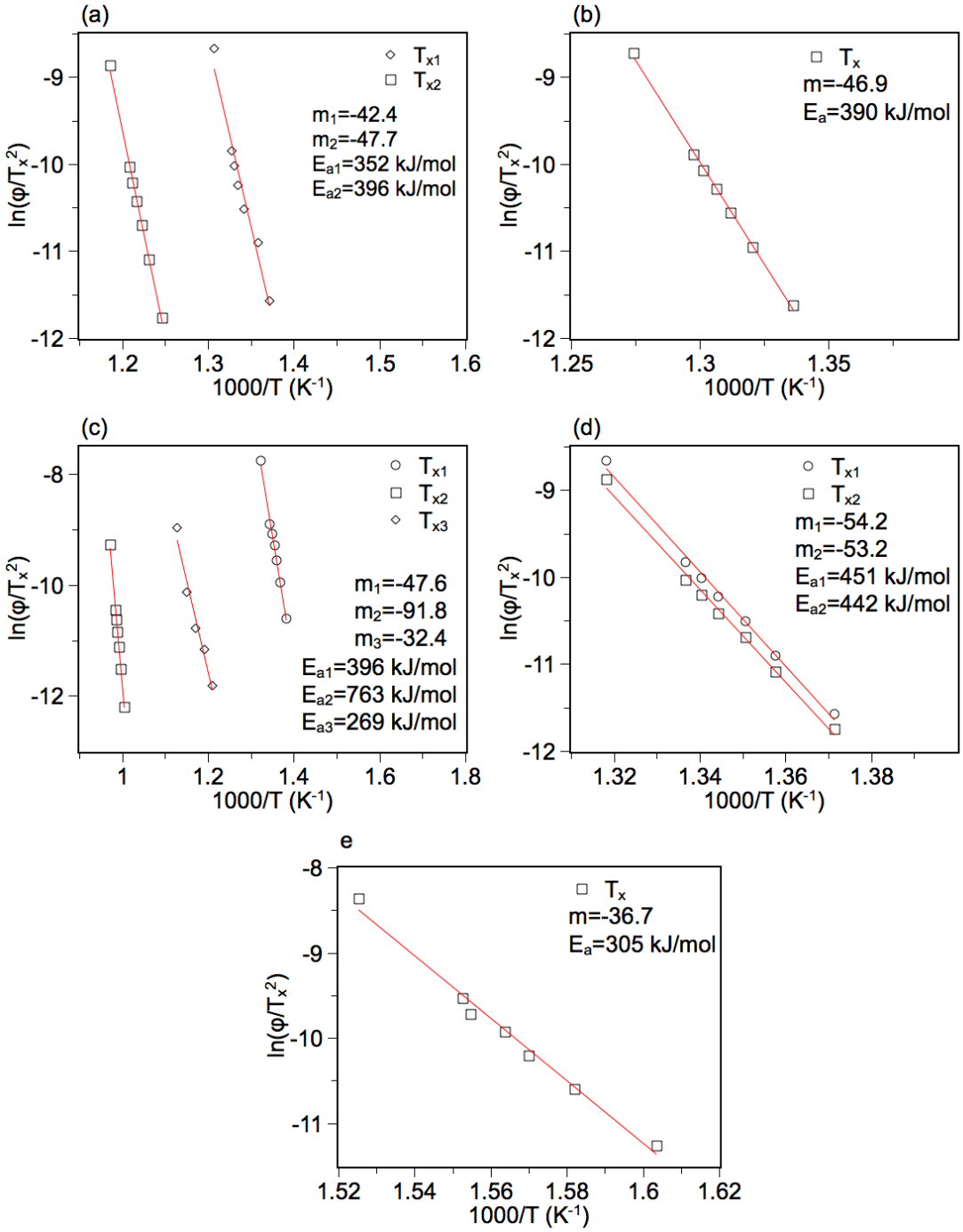

Figure 15: Activation energy of (a) Ni1 ($Ni_{40}Fe_{40}Si+B_{19}Mo_{1+2}$), (b) Ni2 ($Ni_{78}B_{14}Si_8$), (c) Ni3 ($Ni_{75.47}Cr_{19}Si_{4.5}Fe_{4.2}B_{2.8}C_{0.03}$), (d) Ni4 ($Ni_{72.12}Cr_{19}Si_{7.3}B_{1.5}C_{0.08}$), (e) Ni5 ($Ni_{88.9}P_{11}C_{0.1}$).

Table 2: Slope and activation energy of the five Ni-based foils

	Ni1	Ni2	Ni3	Ni4	Ni5
m_1	-42.4	-46.9	-47.6	-54.2	-36.7
E_{a1} (kJ/mol)	352	390	396	451	305
m_2	-47.7		-91.8	-53.2	
E_{a2} (kJ/mol)	396		763	442	
m_3			-32.4		
E_{a3} (kJ/mol)			269		

3.2 X-ray diffraction patterns

As shown in Figure 17, free sintering and SPS exhibited different crystallization products and kinetics, even at the same temperature. The primary phase obtained from the XRD pattern varied with sintering methods. For SPS samples (see Figure 16), $Fe_{0.95}Si_{0.095}$ was the primary peak for samples with sintering temperature at T_x+10 K and T_x+20 K. When the sintering temperature increased to T_x+30 K, there were two strong peaks appearing, $Fe_{19}Ni$ and $(Fe_{19}Si)_{0.1}$. Since the peak positions of $Fe_{0.95}Si_{0.095}$ and $(Fe_{19}Si)_{0.1}$ were so close, and the sample surface was not perfectly flat, those two peaks could be the same one. At T_x+10 K, most of the foils were still amorphous with only one sharp peak, $Fe_{0.95}Si_{0.095}$. At T_x+20 K, Ni_4B, $MoNi_4$ and Ni_2Si started to appear as secondary phases. At the highest experiment temperature, the primary phase was FeNi, indicating that Fe-Si compound obtained before could be a metastable phase. As the temperature increased, the crystallization kinetics enhanced greatly and the

metastable phases became minor. Therefore FeNi could be treated as the ultimate stable phase.

For free sintering samples, the sample started to devitrify at lower temperatures and the resulting phases were more complicated. At T_x+10 K, $(Fe_{19}Si)_{0.1}$ (α-Fe with little Si solid solution), $Ni_{31}Si_{12}$ and MoNi appeared simultaneously. However, MoNi was proven to be a metastable phase as the temperature was higher, so it disappeared after T_x+10 K. At the same time, Fe_3Ni, appeared and had a comparable intensity as $(Fe_{19}Si)_{0.1}$. In addition, $Ni_{31}Si_{12}$ was still detected according to the XRD pattern. However, when the sintering temperature continued to increase to T_x+50 K more $Ni_{31}Si_{12}$ appeared, as more peaks with higher intensity and narrower width were detected in Figure 17. The number of primary peak decreased to just one, which was identical to the situation in the SPS experiment. The intensity of the right-side primary peak ($(Fe_{19}Si)_{0.1}$) was significantly weakened at Tx+50 K, and transformed to FeNiSi. The left side primary peak, given by FeNi, remained at its high intensity and had a narrower peak width as temperature increased.

Among all the XRD patterns, as temperature increased, the stability of Fe-Si compound decreased severely. Si atoms preferred to form a compound with Ni instead of Fe when temperature went beyond T_x+30 K. Therefore it could be concluded that the Fe-Si compound was one of the

metastable phases during the multiple-stage crystallization process while Fe-Ni and Ni-Si were the ultimate stable phases. In addition, the absence of those phases at lower temperature also indicated that the formation of Fe-Ni and Ni-Si phases required higher activation energy, which could not be achieved at lower temperature.

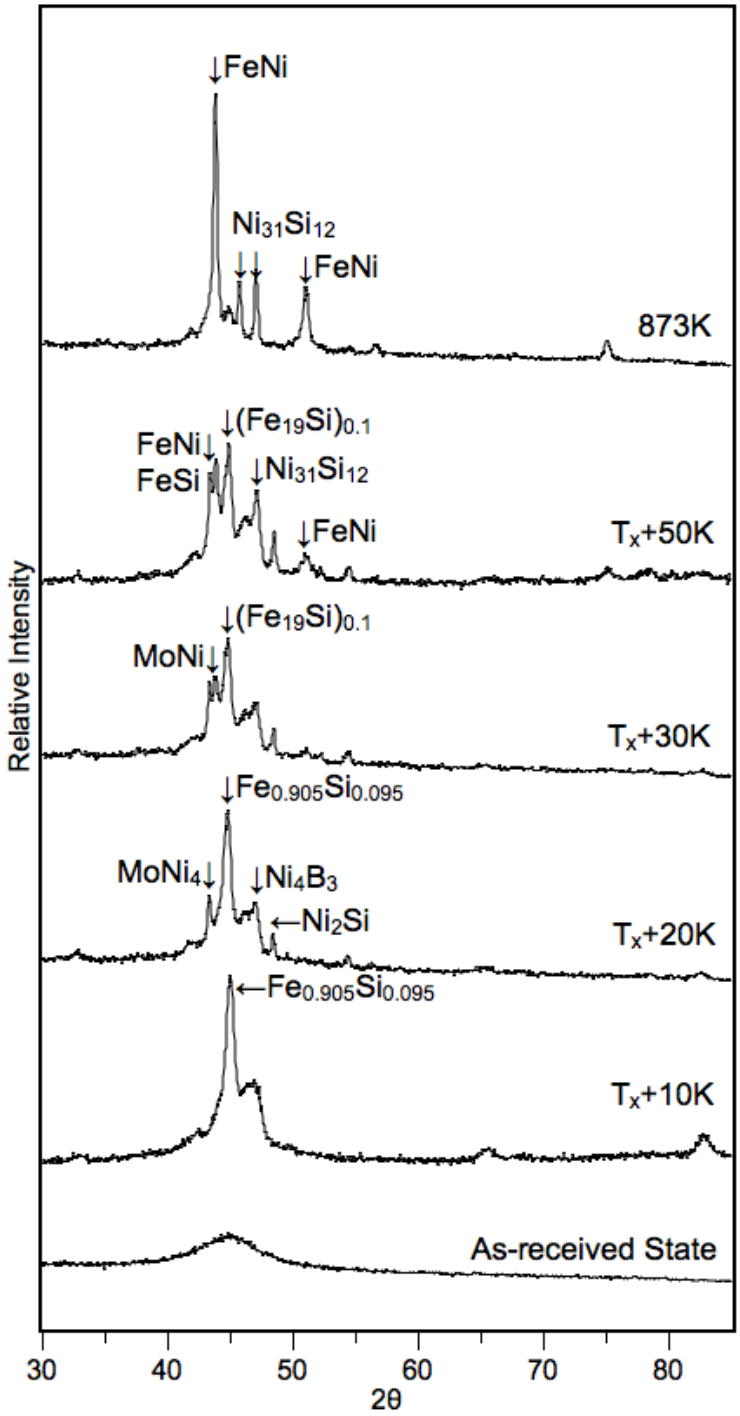

Figure 16: Ni1 ($Ni_{40}Fe_{40}Si+B_{19}Mo_{1+2}$) XRD patterns obtained from SPS samples.

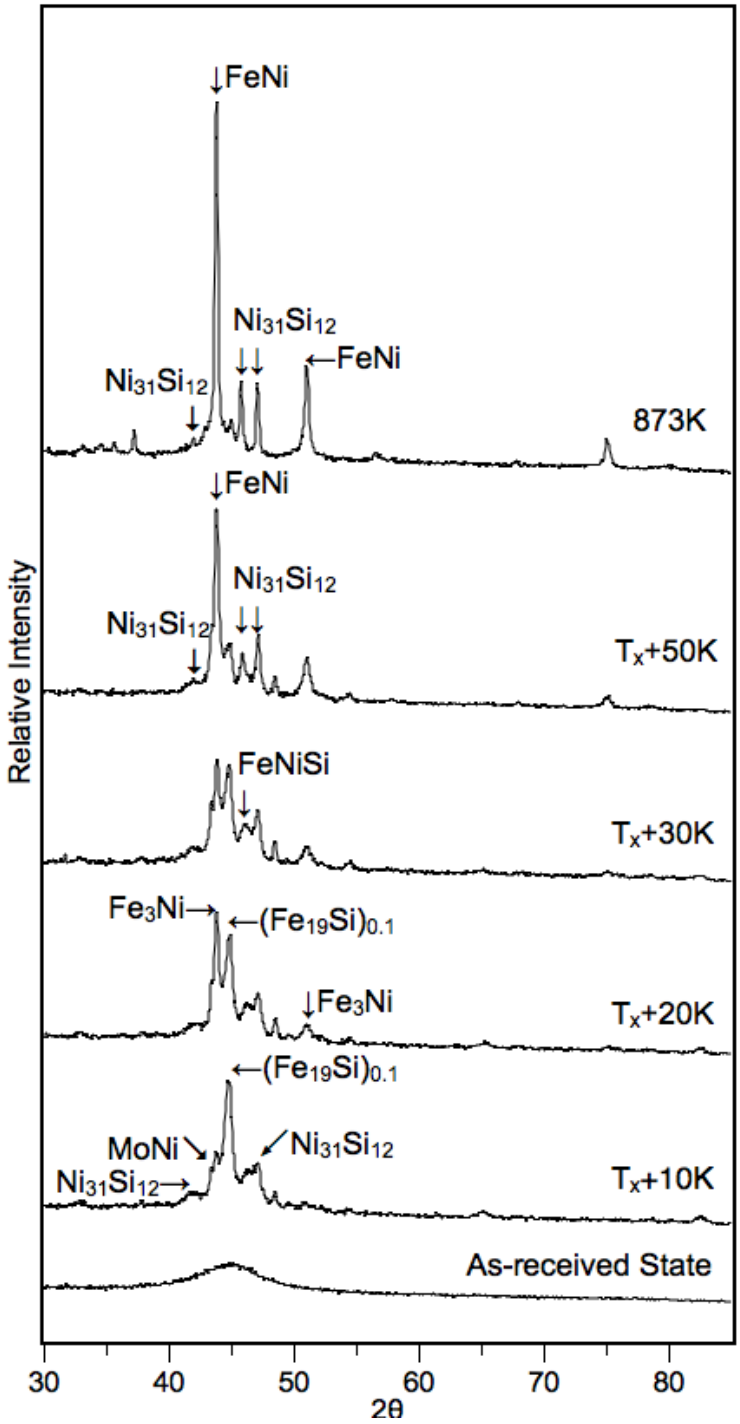

Figure 17: Ni1 ($Ni_{40}Fe_{40}Si+B_{19}Mo_{1+2}$) XRD patterns obtained from pressureless sintering method.

As shown in Figure 18 and 19, the XRD patterns of Ni 2 foils are presented according to the sintering temperatures and sintering methods. According to Figure 20, where sharp peaks could be observed, Ni 2 foils were

not fully amorphous before sintering. They had some extent of devitrification.

For the SPS samples, the XRD patterns (presented in Figure 18) showed that the main two phases obtained were Ni_3B and Ni_3Si. There is no obvious change of the phases among the whole experimental temperatures. In addition, as the sintering temperature increases, the width and the intensity of peaks do not change much from T_x+10 K to 873 K. It might be a result of pre-existing devitrification, so the phases and peak intensity did not change much as for Ni1.

For presureless sintering samples, the same phases were obtained at different temperatures. The insert of Figure 19 showed a close look near the main peak. According to this intersect figure, it was shown that $Ni_{17}Si_3$ and Ni_3Si were the only two phases obtained from free sintering. In addition, the intensity of the peaks in Figure 19 varied. It did not follow the trend that higher sintering temperature results in higher peak intensity. The peak intensity of T_x+20 K and T_x+30 K were even lower than the peak intensity of T_x+10 K, and the peak intensity of T_x+50 K was comparable with the peak intensity of T_x+10 K. It might because the crystallization inside the specimens was not homogeneous. The tested area of T_x+10 K sample was highly crystalline, according to the significant sharp and intense peak shown in Figure 19.

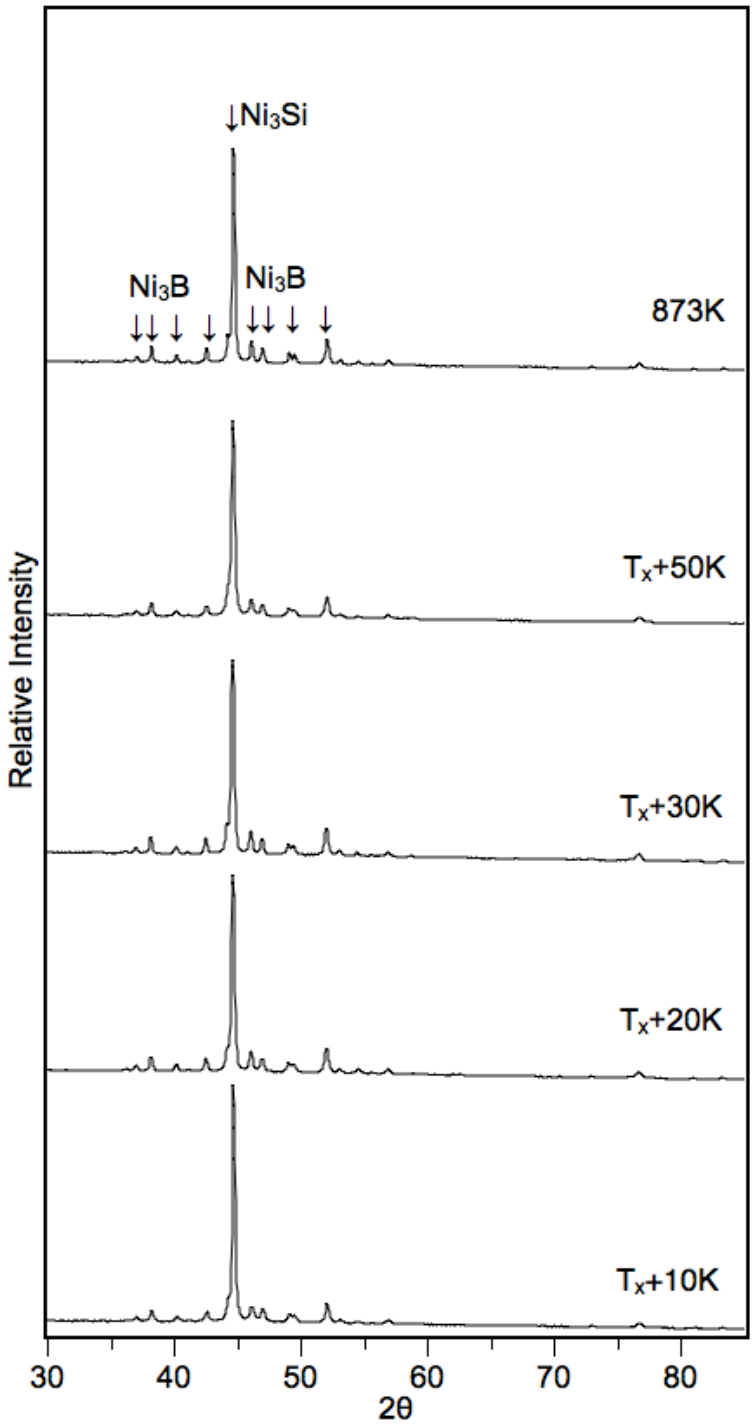

Figure 18: Ni2 ($Ni_{78}B_{14}Si_8$) XRD patterns obtained from SPS samples.

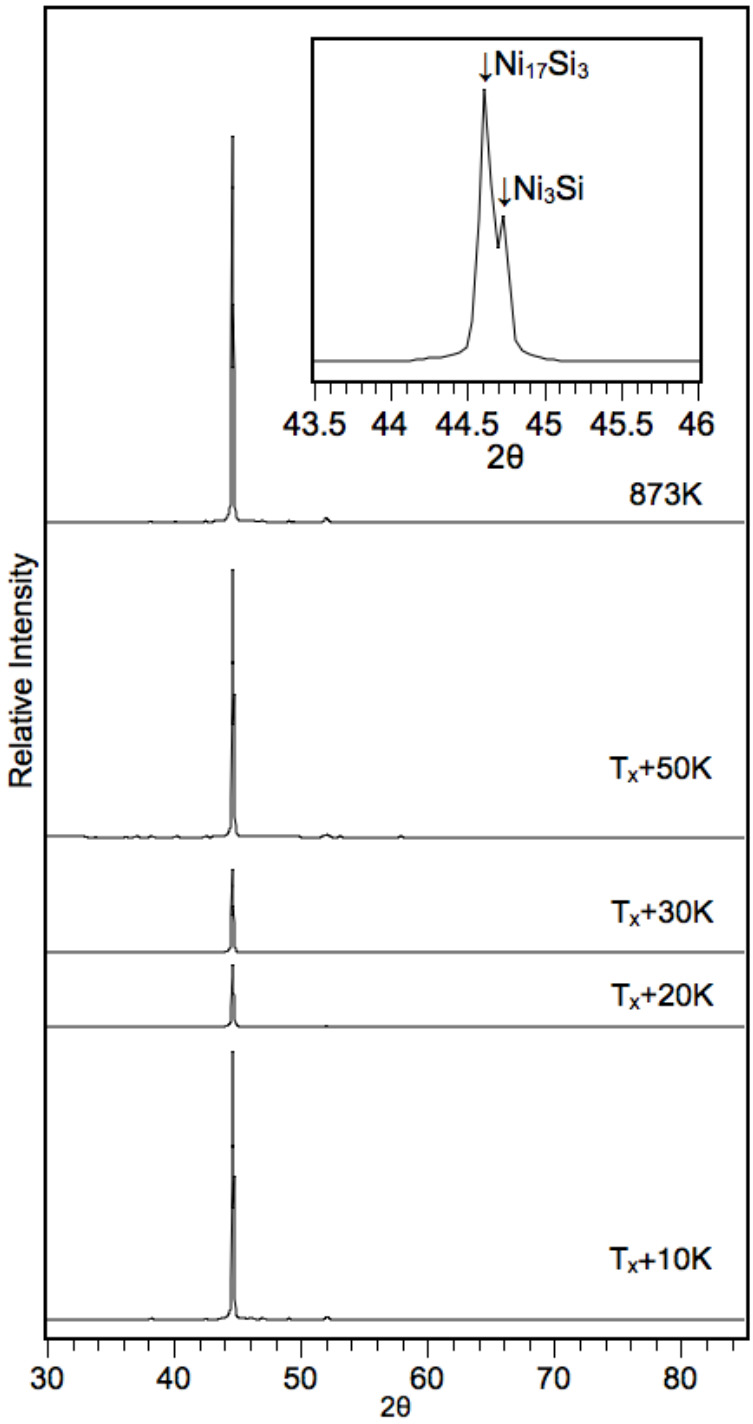

Figure 19: Ni2 ($Ni_{78}B_{14}Si_8$) XRD patterns obtained from pressureless sintering samples.

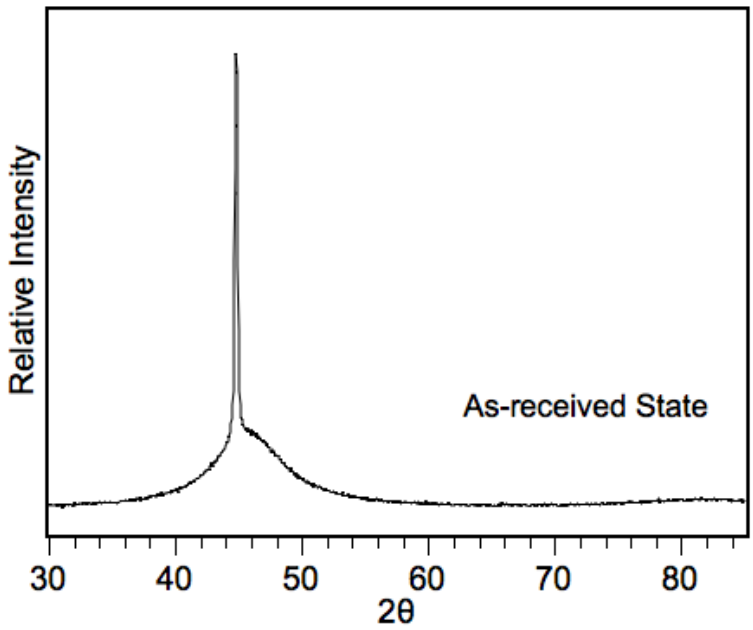

Figure 20: XRD of the as-received Ni2 foils.

For Ni3 SPS samples shown in Figure 21, as the sintering temperature increased, the primary phase changed according to the XRD pattern. At the lowest temperature, T_x+10 K, the primary peak was given by $(Cr_2Ni_{23})_{0.16}$, with some BNi_3 in it. However, when sintering temperature increased, the primary peak intensity became higher, and the shape of the peak changed from small hump to sharp peaks. From T_x+30 K, $Ni_{0.92}Si_{0.08}$ was formed, and BNi_3 started to have peak splitting at 2θ = 47° and 50°.

For the pressureless sintering samples, shown in Figure 22, the phases contributing to the primary peak have also changed as temperature increased. At T_x+10 K, only $Cr_{13}Ni_5Si_2$ contributed to devitrification throughout the sample, within the XRD detection limitation. BNi_3 peaks near 2θ = 47° and 50° could be detected, but it was still amorphous according to the peak shape. When sintering temperature increased 10 K higher, the

primary peak changed to $Ni_{0.92}Si_{0.08}$, and the previous $2\theta=53°$ peak was also contributing to $Ni_{0.92}Si_{0.08}$. It was obvious that when the sintering temperature continued increasing, Si preferred to formed a compound with Ni, instead of Cr. This indicated the higher stability of Ni-Si compound, while Ni-Cr might be the metastable phase during the crystallization process. In addition, comparing the two methods at Tx+10 K, Ni-Cr-Si compound was present in the free-sintering sample while SPS only resulted in Ni-Cr compound. The incorporation of Si atoms suggested the Ni-Si phase had the highest stability.

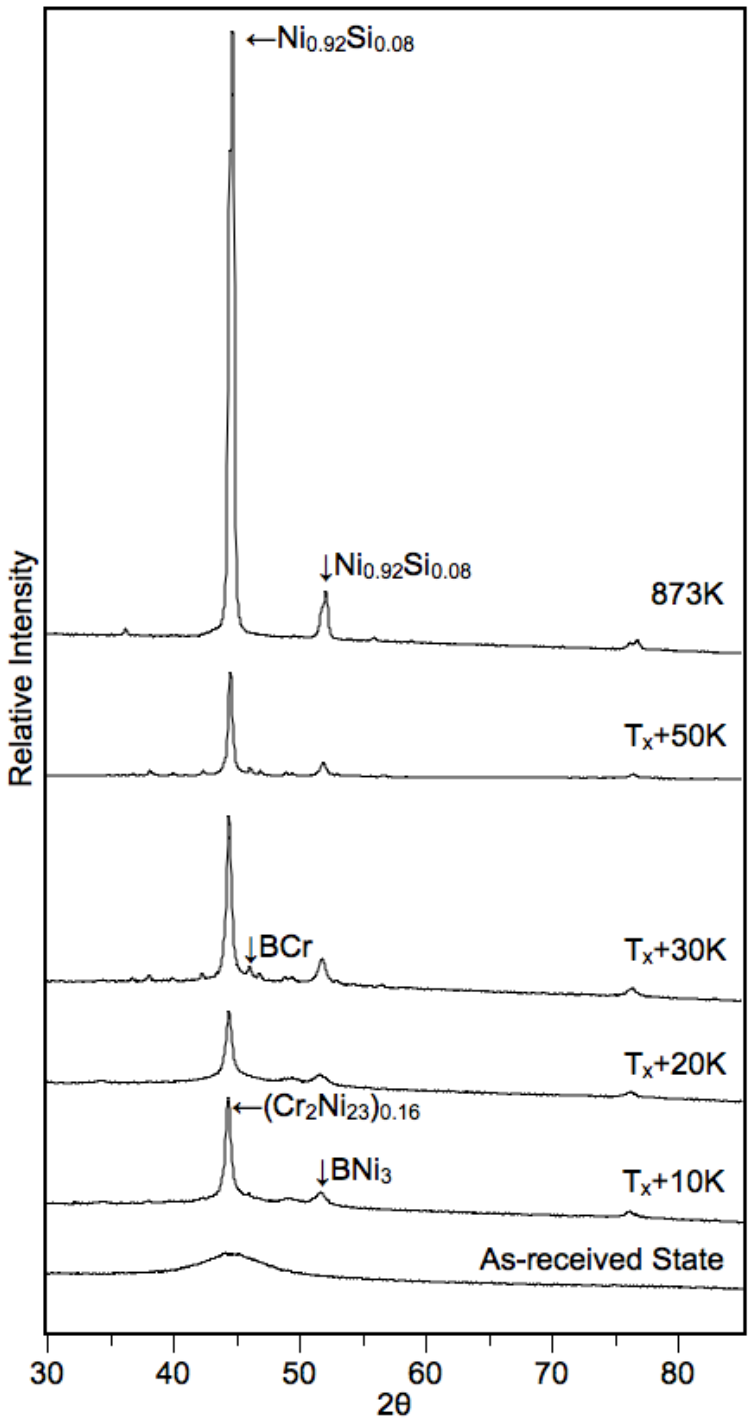

Figure 21: Ni3 ($Ni_{75.47}Cr_{19}Si_{4.5}Fe_{4.2}B_{2.8}C_{0.03}$) XRD patterns obtained from SPS sample.

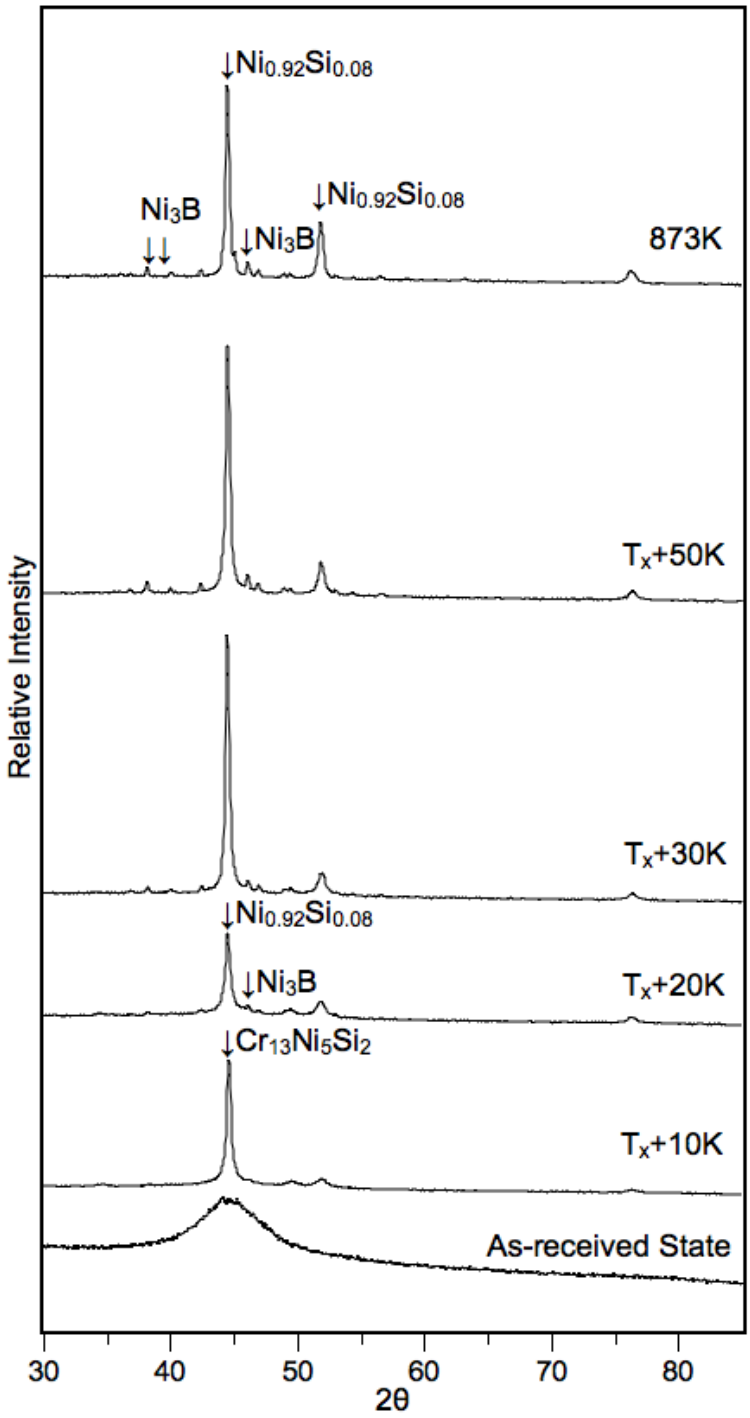

Figure 22: Ni3 ($Ni_{75.47}Cr_{19}Si_{4.5}Fe_{4.2}B_{2.8}C_{0.03}$) XRD patterns obtained from pressureless sintering method.

With a similar composition as Ni3, Ni4 resulted in similar crystalline phases from both SPS and pressureless sintering. As shown in Figure 23, Cr-Ni compound mainly contributed to the primary peak at T_x+10 K, 20 K and

30 K. $(Cr_2Ni_{23})_{0.16}$ was the main crystalline phase at T_x+10 K. However, as temperature increased by just 10 K and 20 K, the relative amount of Cr in the compounds decreased, indicating its metastable nature. Meanwhile, $Ni_{31}Si_{12}$ had a lower and wider peak shape indicating the lower level of crystallinity. When the temperature increased to T_x+30 K, the primary peak was obtained from $Cr_{0.1}Ni_{0.9}$ with some $Ni_{74}Cr_{28}$. As temperature further increased to T_x+50 K and 873 K, all the relative intense peaks were contributed by Ni-Si compound, revealing that it has a greater stability and needs higher activation energy to form.

For the pressureless sintering samples, shown in Figure 24, it basically follows the same phase-development trend as the SPS samples. The samples had the same crystalline phases at T_x+10 K and 20 K. At these temperatures, the primary peak was obtained from $(Cr_2Ni_{23})_{0.16}$, which could be evaluated as Ni crystalline with few Cr dissolved in it. As the sintering temperature increased, the relative amount of Cr increased as well, and Si got involved in compound formation to form Cr_3Ni_2Si. However, when the temperature increased to 873 K, the primary peaks were formed by two kinds of compounds, NiSi and CrNi. Besides the compounds, crystalline Ni and Cr were also detected in the samples. Crystalline Ni showed higher intensity and narrower peak width as the sintering temperature increased. However, Cr stayed partially crystalline until the sintering temperature

increased to T_x+30 K. After that, Cr peak signal became weaker and could not be detected at temperature beyond T_x+50 K. However, when the temperature was raised beyond Tx+20 K, these two sintering methods started to obtain different devitrified phases at the same sintering temperatures. Similar as in Ni3 experiments, Ni-Si had the higher stability than Ni-Cr.

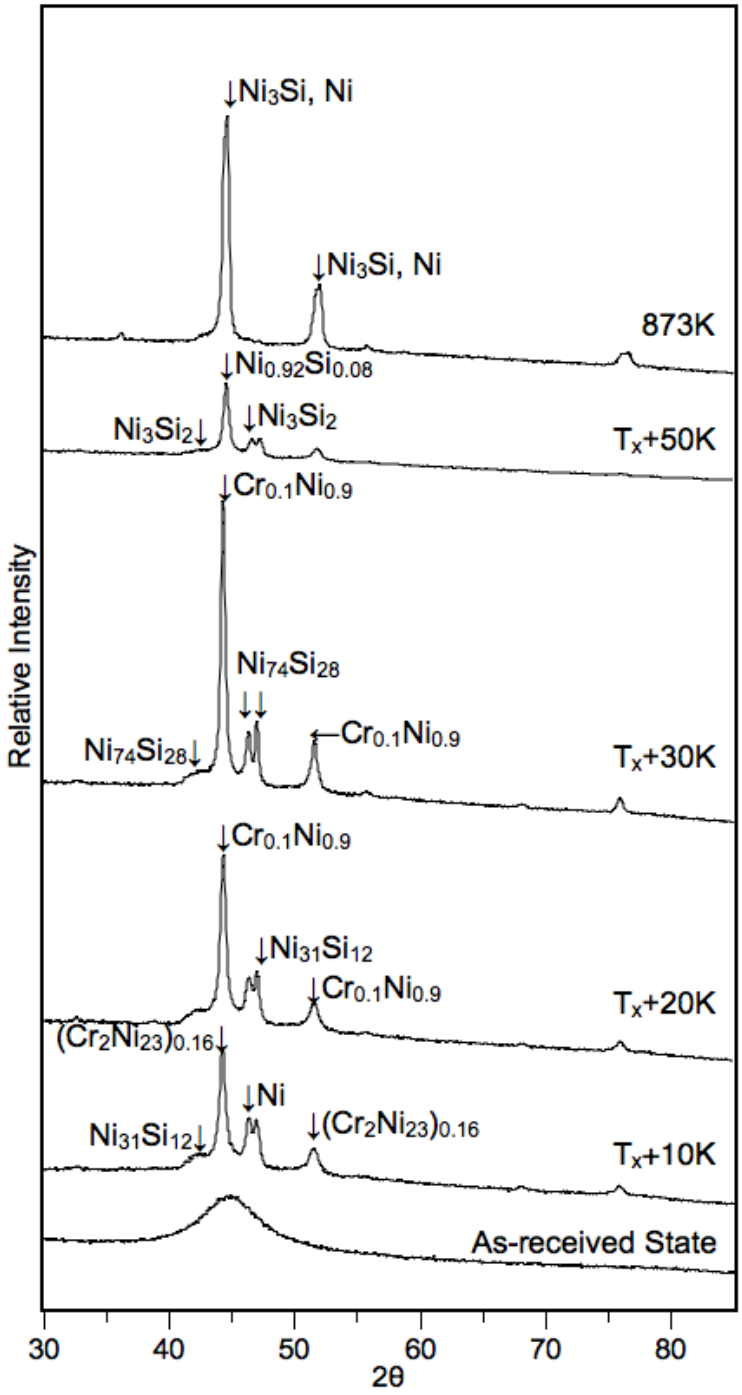

Figure 23: Ni4 ($Ni_{72.12}Cr_{19}Si_{7.3}B_{1.5}C_{0.08}$) XRD patterns obtained from SPS method.

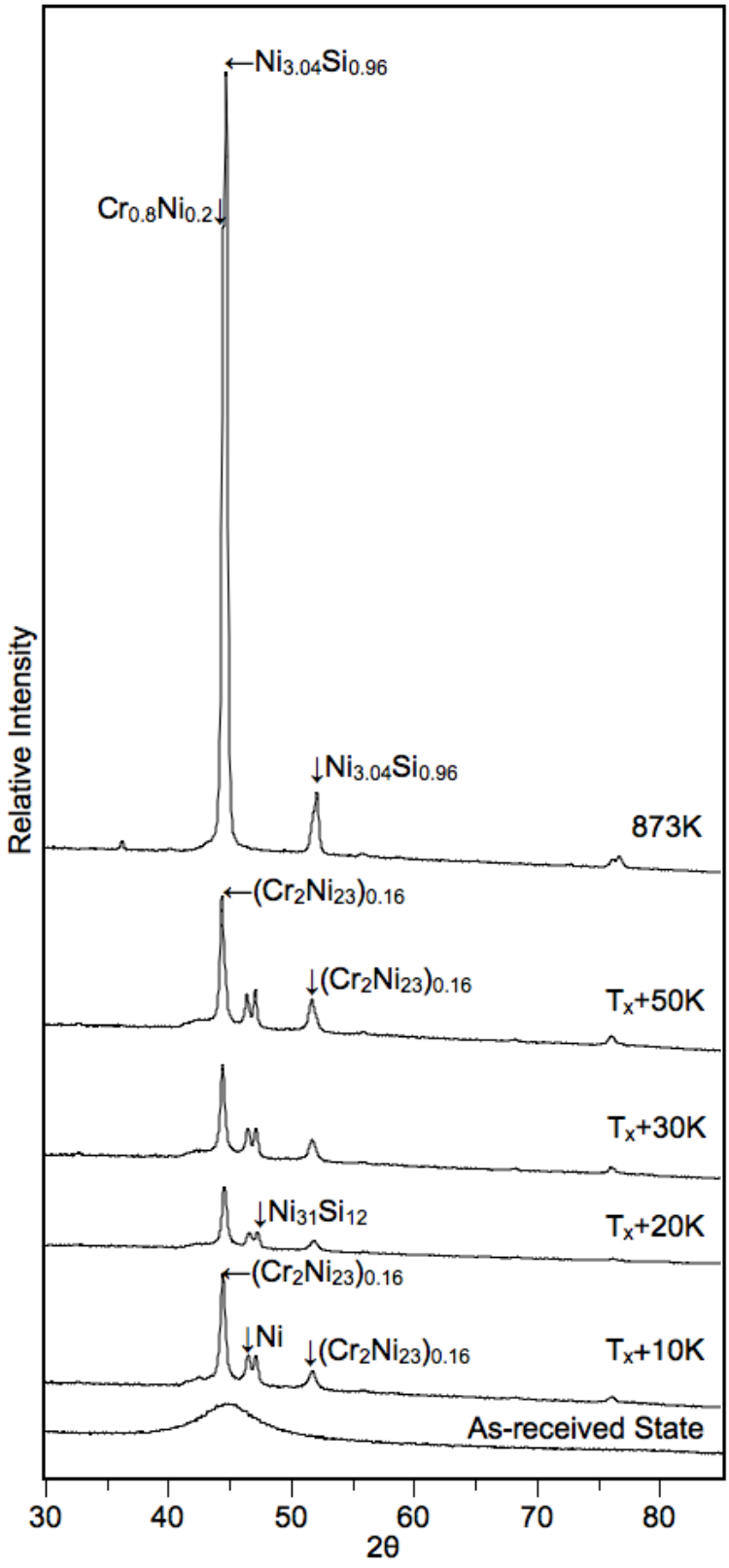

Figure 24: Ni4 ($Ni_{72.12}Cr_{19}Si_{7.3}B_{1.5}C_{0.08}$) XRD patterns obtained from pressureless sintering method.

Considering the composition in Ni5, it is basically Ni and P, with low

amount of C. As a result of that, the products obtained from sintering should be just Ni, P, and Ni-P compound. As shown in Figure 25 and Figure 26, both in SPS and pressureless sintering, Ni5 devitrified significantly from T_x+10 K, and all the patterns had multiple sharp and intense peaks corresponding to Ni and Ni-P compound. From as-received amorphous foil, the highest point of the hump is close to the Ni peak position, indicating that the foil tends to form crystalline Ni. After the sintering process, the Ni peak was detected both at 2θ = 45° and 53° approximately. Among all the experimental temperatures, SPS and free sintering samples followed the similar trend. With SPS method, only at T_x+10 K, Ni_5P_4 phase has been detected, as shown in Figure 25. When temperature increased, it turned to become Ni_3P. Ni and Ni_3P became the only two phases that could be detected. This phase transformation suggested that Ni_5P_4 is a metastable phase that only exists at low sintering temperatures. As sintering temperature increased, Ni_5P_4 would transfer to a more stable phase Ni_3P.

Different from SPS samples, samples sintered without current and high pressure also obtained crystalline P at 2θ = 38° and mixture of Ni_5P_4 and Ni_3P at 2θ = 48°, when sintering temperature was relatively low. However, as sintering temperature increased beyond T_x+30 K, those phases were replaced by Ni_3P and Ni. This phenomenon also suggests that Ni_3P and Ni have higher stability at high temperature, and P and Ni_5P_4 were transitional or

metastable phases. The absence of P peak in SPS samples indicates that thermodynamically, P has the similar ability to form under the same temperature, as Ni_5P_4. However, crystalline P might have lower kinetics, which requires longer reaction time for P atoms to diffuse and form this phase.

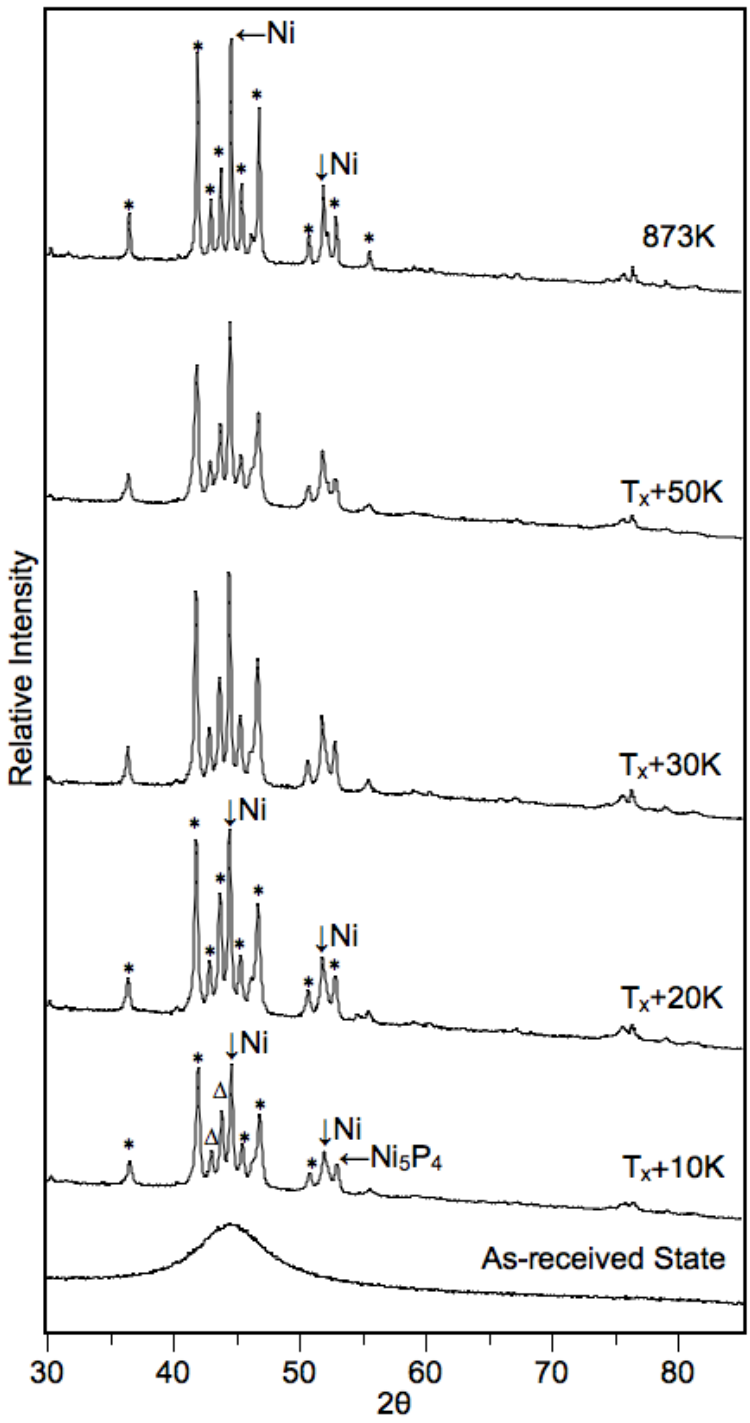

Figure 25: Ni5 ($Ni_{88.9}P_{11}C_{0.1}$) XRD patterns obtained from SPS method.

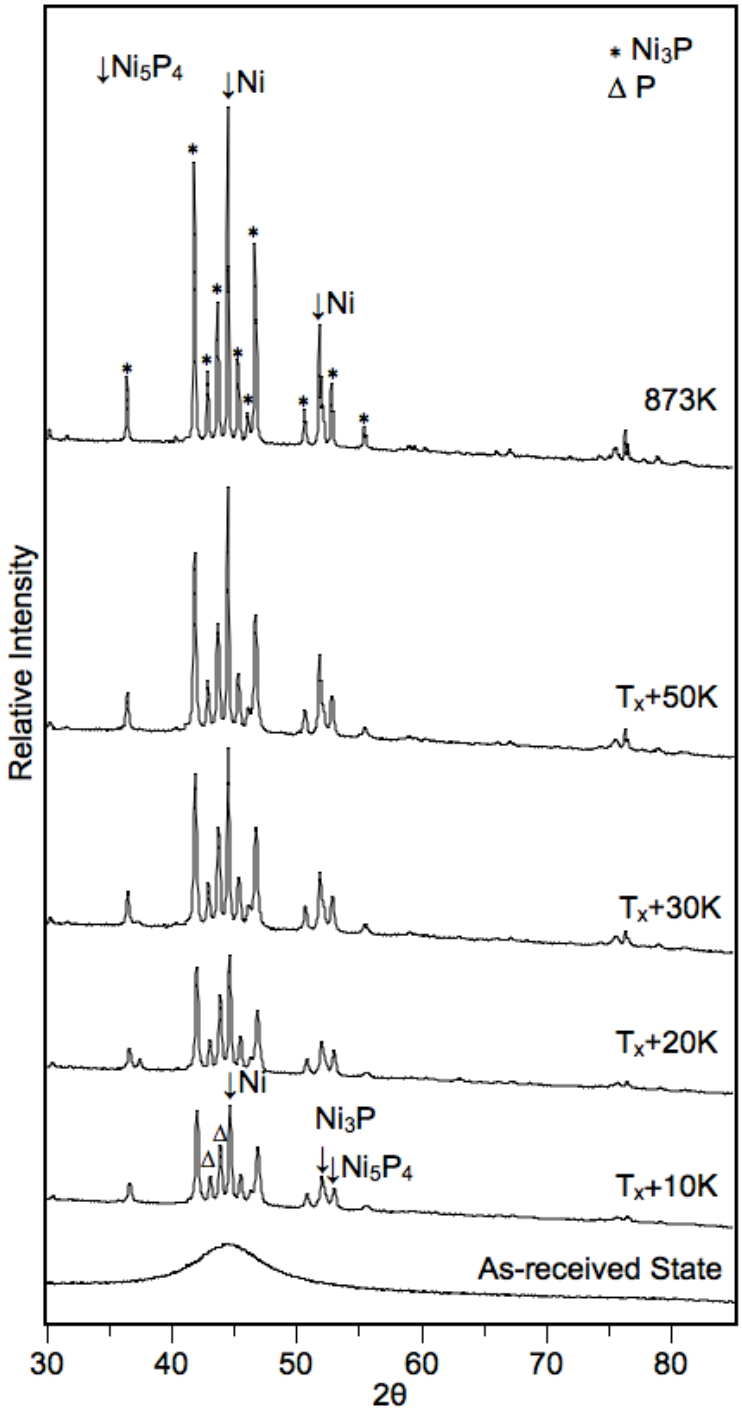

Figure 26: Ni5 ($Ni_{88.9}P_{11}C_{0.1}$) XRD patterns obtained from pressureless sintering method.

Generally, the FWHM value decreased when sintering temperature increased. This trend corresponds to the narrowing peak width observed in XRD pattern (Figure 16-26). However, the decreasing trend of FWHM does

not follow a linear or logarithm function. According to the multiple crystallization processes observed in DSC curves, it is believed that the FWHM trend has a close relationship to those multiple exothermic reactions occurring during the sintering process. Based on the consideration of that, the onset temperatures of each exothermic reaction were labeled in the map with dashed lines. Since the sintering temperatures are all above the crystallization temperatures of each Ni foil, the labeled onset temperatures start with T_{ox2}. The amount of different stages of crystallization depends on the materials natural properties. Besides sintering temperature, applied pressure, current assisted sintering condition and holding time are other three crucial factors that need to be taken into consideration.

Among those five foils, only three FWHM maps were obtained, because the other two foils have overlapped primary peaks. As a result of that, a complete FWHM map could not be obtained. In Figure 31(a), FWHM of Ni2 did not change significantly along the whole experimental temperature range. It was within the expectation that Ni2 was not completely amorphous before sintering. According to the XRD pattern shown in Figure 20, it had an intense and sharp peak, indicating its partial crystalline state. In SPS, it basically remains at the similar FWHM value. However, in pressureless sintering case, the FWHM reduced slightly as temperature increased. Certainly, the average FWHM of free sintering was higher than SPS, due to

the much longer reaction time. This suggests the different crystallization kinetics in these two sintering methods.

In Figure 31(b), it was obvious that FWHM from both sintering methods reduced with rising temperature. However, the reduction rate of these two methods was different. At low temperature, the FWHM value of free sintering was smaller due to the longer crystallization time. However, as the sintering temperature increased, the FWHM value of SPS dropped faster, as it was getting closer to free sintering data under the same experimental temperature. SPS was the one that had higher reduction rate of FWHM value, indicating SPS higher crystallization kinetics. Similar in Figure 31(c), Ni5 exhibited the decreasing FWHM value trend as sintering temperature increased. In addition, the FWHM values of the two sintering methods were getting closer as temperature raised. However, at 873K, the FWHM value increased by a small amount. It might be caused by experiment error, since the value is small. In addition, several relatively intense peaks appeared within a narrow range that could possibly influence the peak shapes, which might contribute to the inaccurate measurement of the FWHM values.

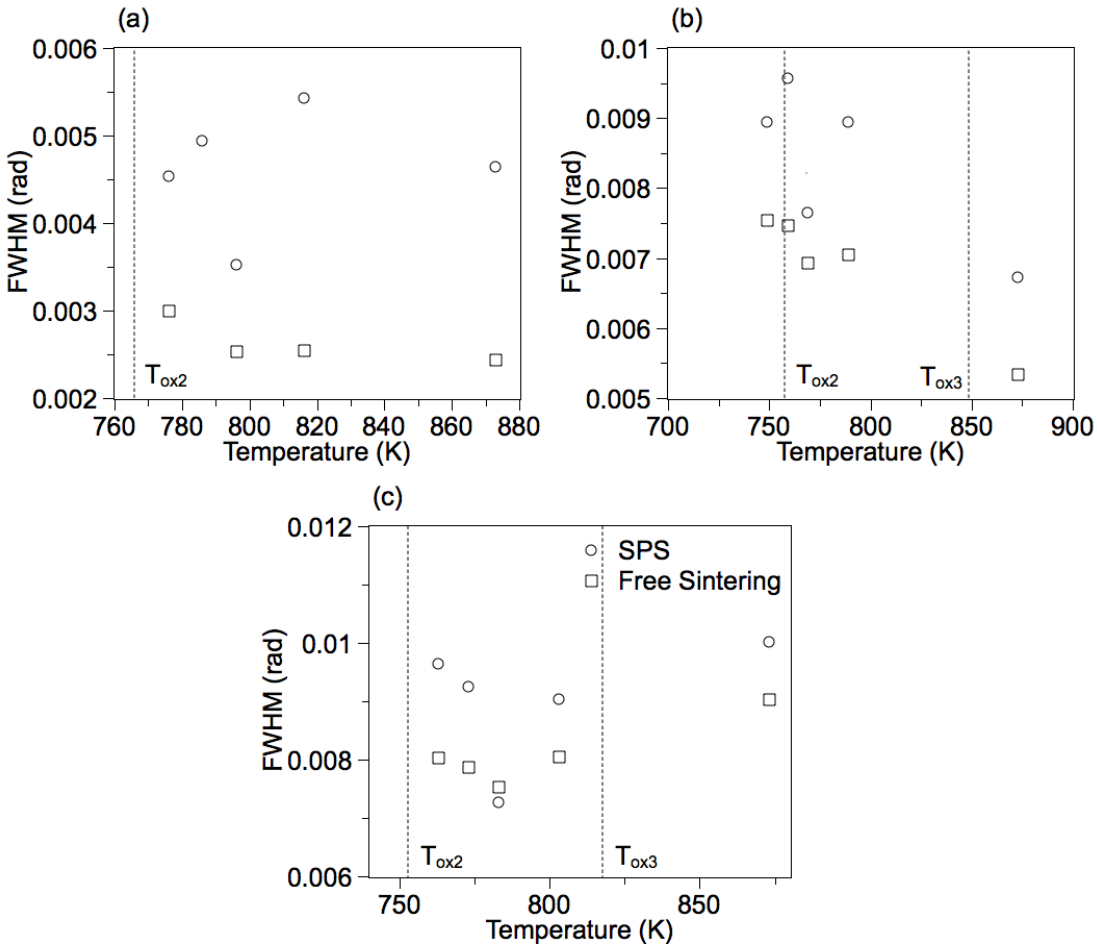

Figure 27: Ni-based samples Full-Width-Half-Maximum (FWHM) map sintered by SPS and pressureless sintering for: (a) Ni2, (b) Ni3, and (c) Ni4.

3.3 Scanning electron microscopy (SEM) characterization

After a carefully polishing process, samples with smooth interfaces were analyzed by scanning electron microscope (SEM) to look at the microstructure of their cross-sections and interfaces between each foil. SEM images of Ni2 SPS sample sintered at T_x+10 K were shown in Figure 28, and its corresponding EDX result is shown in Figure 29.

As shown in Figure 28(a), T_x+10 K resulted in poor bonding results, since it was sintered at relatively low temperature compared to the whole

experimental range. Between those two foils, there is a porous, fragile, and thick interface. The thickness of the interface was approximately 7 μm. Diffusion phenomenon could be observed at both edges of this interface. In the surface of foils, unique morphology with lighter contrast could be observed. Generally, those patterns exist along the foil. However, with closer observation, as shown in Figure 28(b), it has radial pattern, which spreads into different directions. In Figure 28(c) and (d), another region with thinner interface has been shown. Figure 28(d) is the image with higher magnification taken in the same area as Figure 28(c). In this region, similar morphology has been obtained. Considering the fact that the sample has been finely polished, the surface of each sample should be flat, without any fringe or folding. It could be concluded that the contrast difference presented in those unique defects should not be result of mechanical deformation. In addition, the radial pattern indicates that these defects should not come from polishing. The other possible reason includes polishing suspension residual, during an initial stage of oxidation. Under the consideration of that, EDX mapping has been done on this specific area. As shown in Figure 29(b), the red spots represented carbon, and the green spots represented oxygen. Both of them have distributed homogeneously across the whole testing region. This indicates that oxidation and suspension residual happened in this area, but neither of them contributed to

the defects near interface. Reviewing all the factors in this experiment that might have effect on it, applied electric current is the only possible reason that resulted in this kind of radial defects.

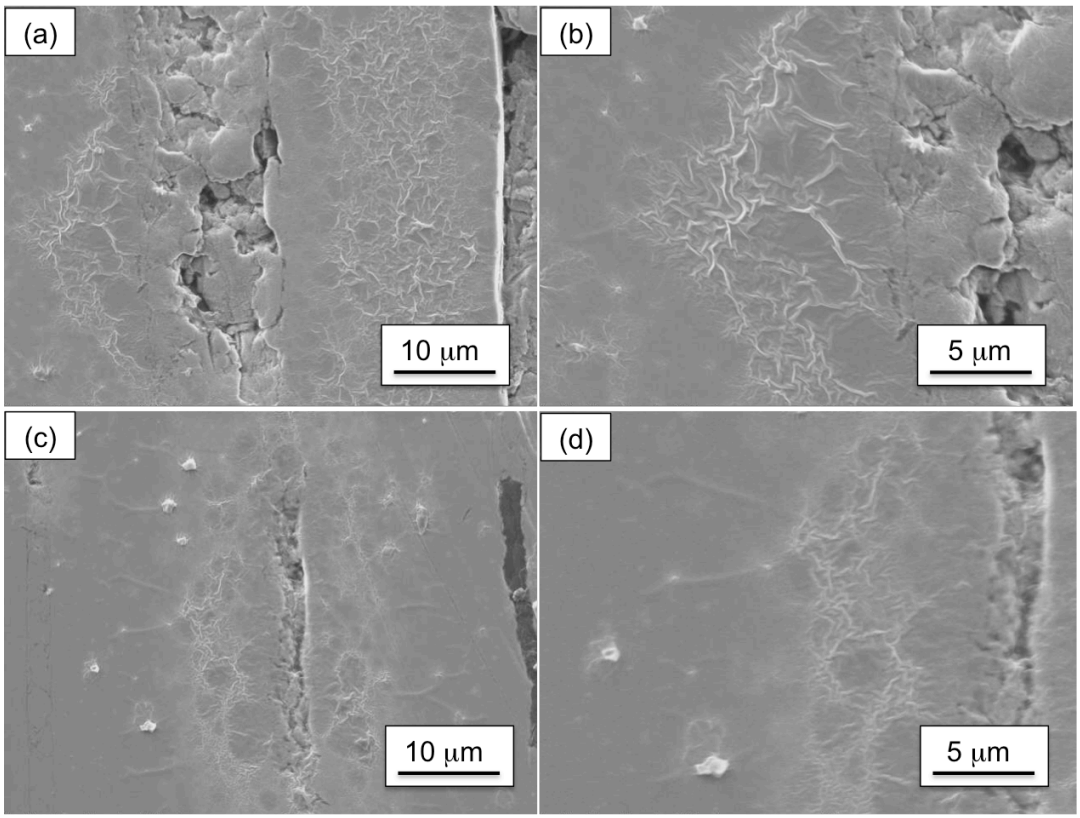

Figure 28: SEM images of Ni2 SPS sample sintered at T_x+10 K, and held for 20 min

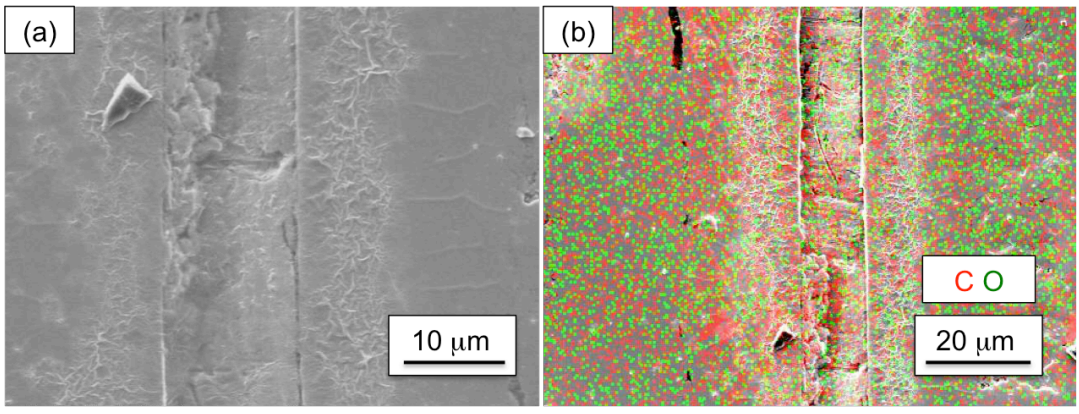

Figure 29: (a) SEM images of Ni2 SPS sample sintered at T_x+10 K, for 20 min, (b) and its corresponding EDX image

In Figure 30, Ni2 SPS sample sintered at T_x+20 K was imaged by ESEM. As shown in Figure 30(a), the whole sample was basically sintered together, but not really well. There are several regions on the right hand side, where pores are present. Since the sample was embedded in the epoxy, margin area of the image was not stable due to overcharging under electron beam during the imaging process. In Figure 30(b), a higher magnification picture was exhibited. It could be seen that there was a thick interface, approximately several micrometers, formed between two foils. In some poorly sintered areas, those interfaces were thick, not flat as the surrounding foils. In addition, the morphology of those interfaces seemed like a result of diffusion process during sintering, trying to bond two foils together. However, in those well-sintered areas, thick interfaces also could be found, but the morphology of the interface was different with those poorly sintered areas, as shown in Figure 30(c). In Figure 30(c), a typical bonding interface was shown with the corresponding labels. It was an interface that tried to close the gap between two foils, but not complete. In addition, there were also surface defects, which had different contrast shown on the surface of the foils. As shown in the Figure 30(d), it was a higher magnification image of the circled area in Figure 30(c). It could be seen from Figure 30(d) that those defects had a thunder-like morphology, and the approximate width of them were several hundred nanometers. The size of these defects

excluded the possibility of grain boundary, and the morphology of them made us believe that it had close relationship with current effect, since high intensity electrical current flew perpendicularly through the sample during SPS.

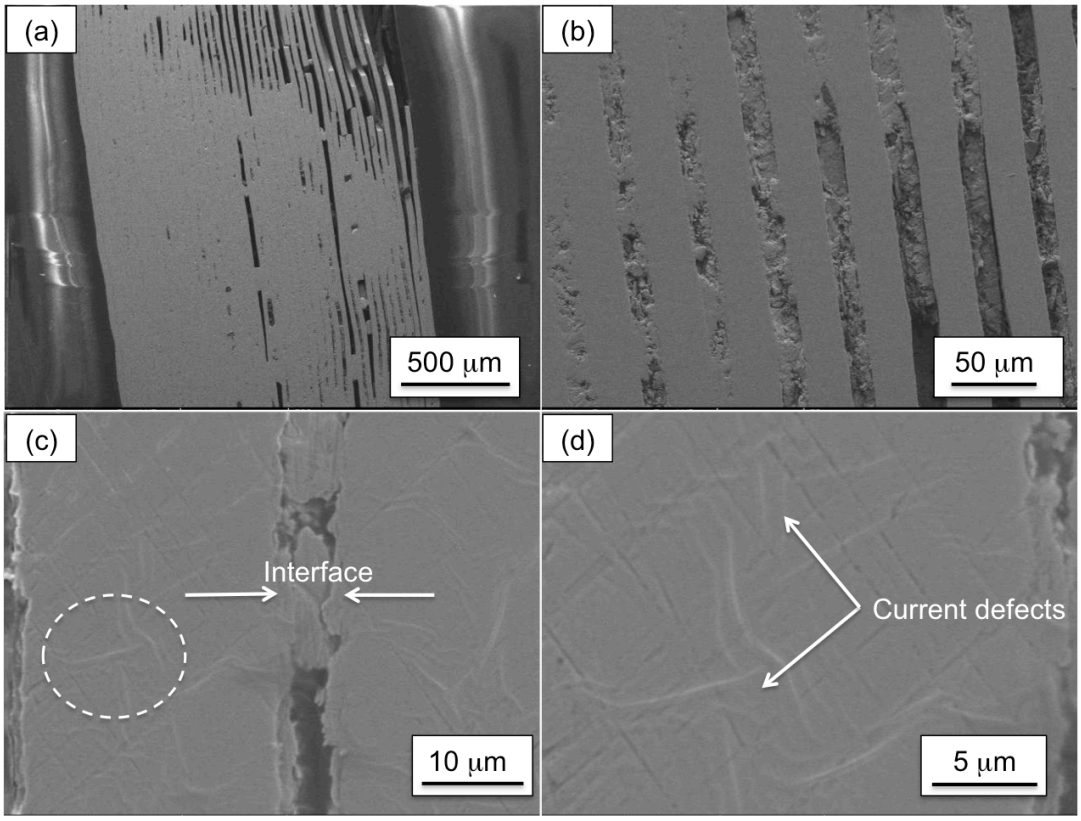

Figure 30: SEM images of Ni2 SPS sample sintered at T_x+20 K, and held for 20 min.

Ni2 SPS sample sintered at T_x+50 K was shown in Figure 32. As shown in Figure 32(a), the extent of bonding in this sample did not show significant improvement, compared to samples sintered at lower temperature. The delamination happened in this sample might have came from the polishing process. Since the sintering temperature in SPS was relatively low

compared to the conventional hot pressing, the bonding obtained would be fragile and sensitive to cracks. When the sample was put onto polishing machine and ground with sand paper, a crack might be formed in epoxy around it, and resulted in delamination of the whole sample.

Regardless, similar defects as in Figure 30 have been observed in this sample. Especially in the region near interface, those defects have extremely high density and significant presence of radial pattern. As shown in Figure 30(c), some part of the defects extended into the interface area. It seemed like this defect had a positive effect on the bonding process.

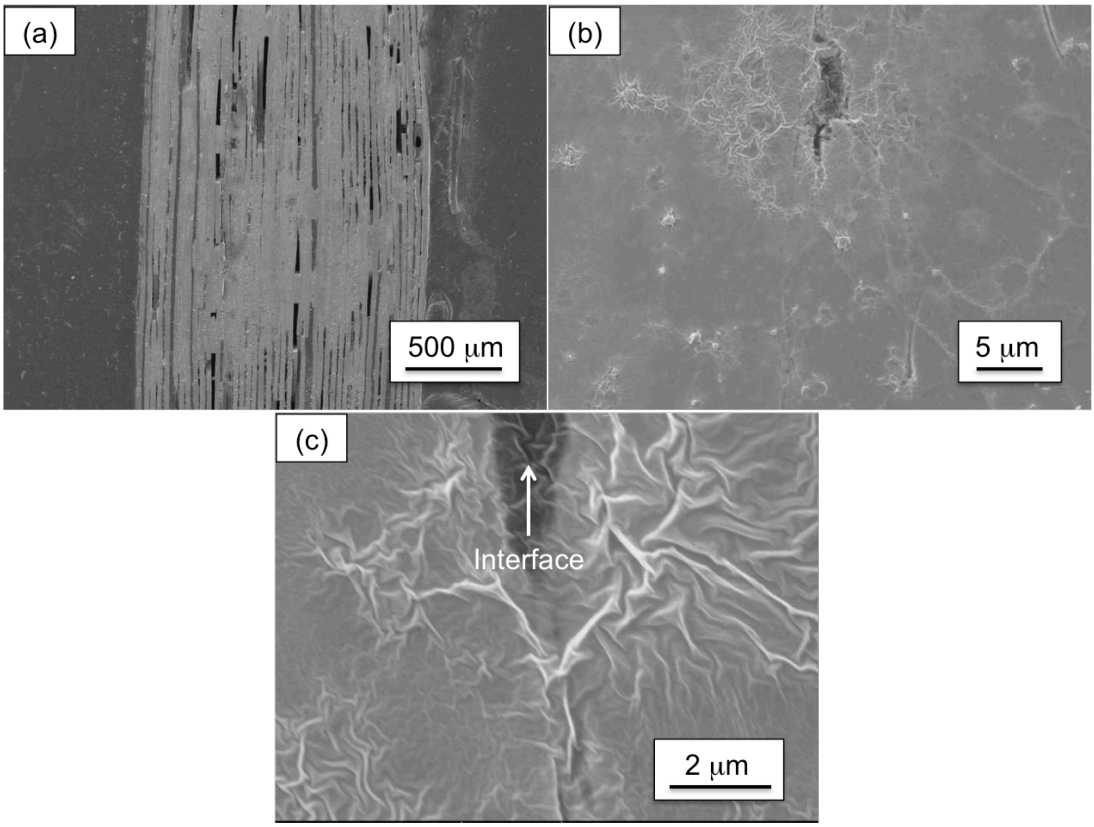

Figure 32: SEM images of Ni2 SPS sample sintered at T_x+50 K, and held for 20 min

In Figure 33, the Ni2 sample sintered at 873 K (600°C) was observed

under SEM. In comparison to the significant amounts of defects observed in previous Ni2 samples, this sample tended to have fewer defects, and their area was much smaller than in previous samples. Besides defects, the bonding condition of this sample was better than that of the previous ones due to the dramatic increase of sintering temperature. In addition, the interface shown in Figure 33(a) and (b) had less pores and gaps. They were close to flat and formed a completely solid interface. This indicated that those unique defects preferred interfaces that were porous, poorly sintered. If the sample was close to solid and well bonded, those defects no longer existed.

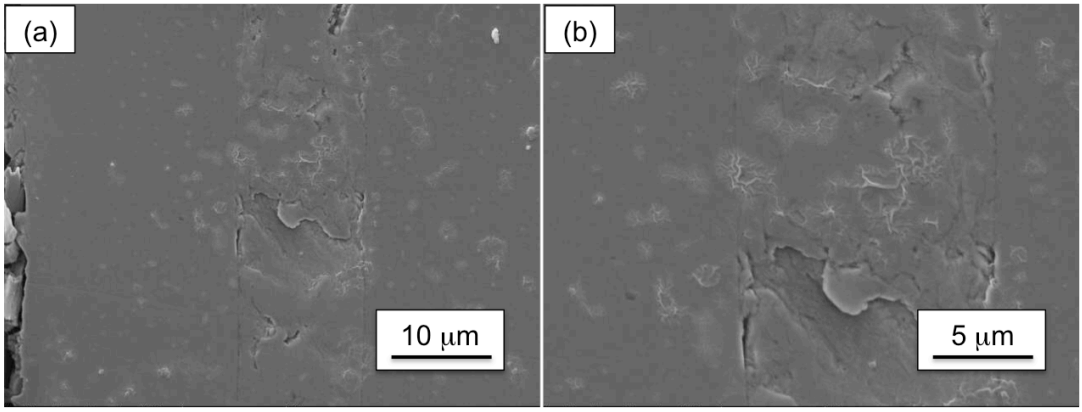

Figure 33: SEM images of Ni2 SPS sample sintered at 873 K, and held for 20 min

Similar to the Ni2 sample, the Ni3 sample was not completely sintered together at T_x+10 K, as shown in Figure 34(a). There were still pores and unbonded foils existing according to the SEM image. Besides unbonded gaps, there were several foils broken down, causing a roughened surface. The high pressure applied in SPS, and the brittle nature of amorphous foils

might be the causes for these observed breaks. In Figure 34(b), the interface between two foils was shown with current surface defects. The approximate thickness of the interface was 5μm, and the width of the current defects was about 500nm. From the morphology of those defects, it looked as though the electric current had assisted two foils in diffusing and forming this thick interface. Similar to other current defects observed in previous samples, those current defects had brighter contrast and continuous morphology throughout the one interface and two surrounding foils. Besides the defects observed in Figure 34 (b), other defects with different morphology have also been observed near cracks in the interface, as shown in Figure 34 (c) and (d). Figure 34(d) was the higher magnification image of the circled area in Figure 34(c). In the middle of the interface in Figure 34(c), there was a crack growing perpendicularly. At the end of the sintering process, SPS would be switched off and the sample would be cooled down without manual control. Considering this situation, the crack might also be caused by the high cooling rate. In addition, the interface formed in sintering might had slightly different thermal expansion coefficient than the rest of sample. Heterogeneous material distribution and high cooling rate would work together to cause thermal shock, resulting in cracks on the interface. Different from the previous ones, the defects observed in Figure 34(c) and (d) had darker contrast, different width and differing morphology. They did not

have continuous paths throughout the interface and foils. Instead, they remained at the edge of the crack, inside the interface. According to the previous research paper by Gilbert on deformation mechanism,[39] those defects have a similar morphology as the deformation images shown in their paper. As a result of that, those defects might be caused by deformation, not current.

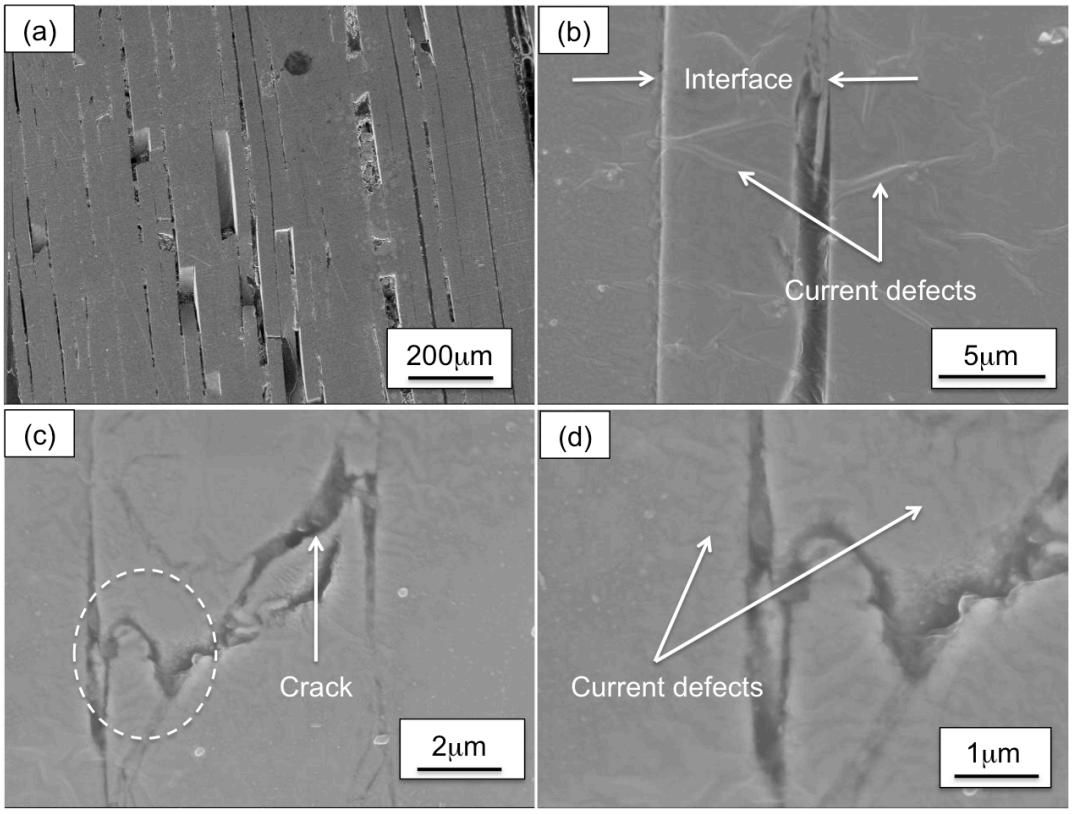

Figure 34: SEM images of Ni3 SPS samples sintered at T_x+10 K, and held for 20 min.

In Figure 35, a variety of images of Ni3 SPS sample sintered at Tx+20 K were presented. Figure 35(a) was a full-view of the sample, indicated that it was sintered a little better than Ni 3 sample sintered at Tx+10 K (see Figure 34(a)). It was within expectation due to the higher sintering temperature.

Similar to Figure 34(b) and (c), in Figure 35(b), there was also an interface that had several micrometers thickness. This might be a result of enhanced diffusion process occurred during the SPS process. In Figure 35(c) and (d), current defects near interface were shown. Figure 35(d) was a closer look of the circled area in Figure 35(c). The morphology of those current defects was similar as in Figure 28(b) and 26(c), which had brighter contrast and all the current defect paths spread out from the center of it. This indicated that the mechanism of these current defects formation might be the same as in Figure 28(b) and 26(c), where different Ni-based amorphous metal foils were used for sintering. As shown in Figure 35(d), as the current defect paths spread into different directions, the size of them, particularly the width of each path, decreased. This possibly had a relationship to the surface energy distribution near this interface. In the center of the current defects, the surface energy might be the highest. Then as the current defect paths moved to the edge area, the surface energy decreased and fewer amount and smaller size of current defects were formed. To prove this, further characterization was required.

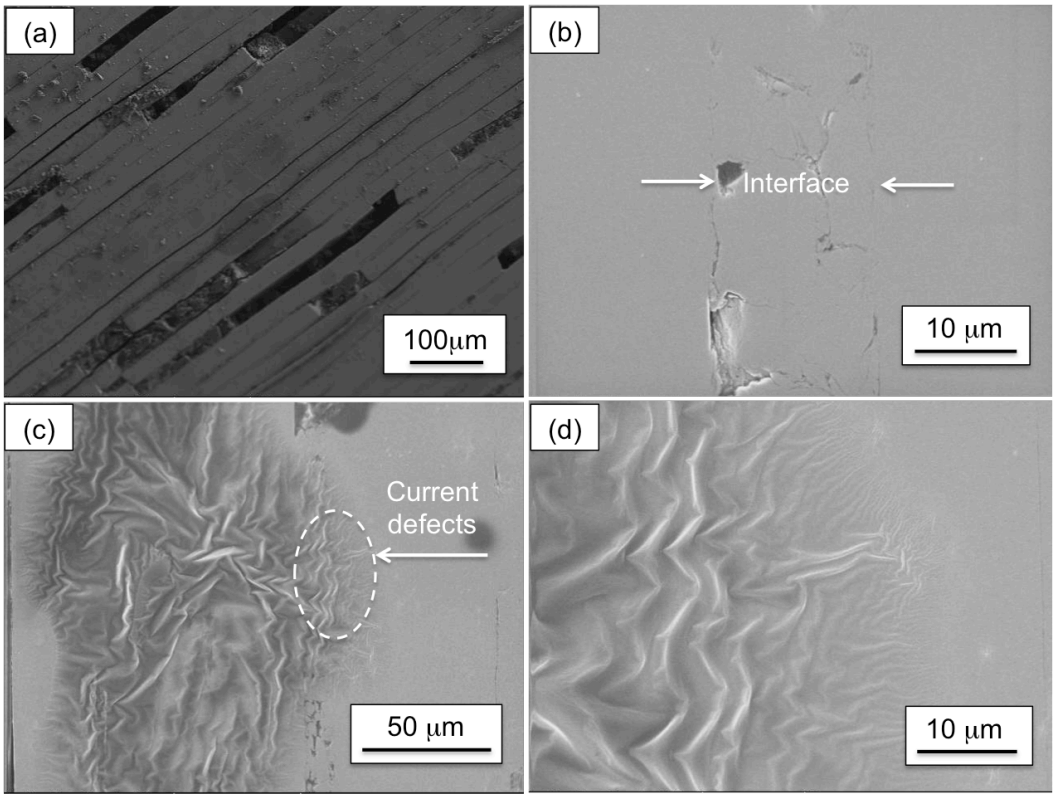

Figure 35: SEM images of Ni3 SPS samples sintered at T_x+20 K, and held for 20 min.

Ni3 SPS sample sintered at Tx+30 K was analyzed by SEM, and the images with different magnifications were present in Figure 36. In Figure 36(a), better sintering and bonding were obtained due to the higher sintering temperature. On the right side of this image, it could be seen that several foils were sintered together firmly and solid, with only tiny gaps between them. In addition, on the left edge of this image, there was some impurity left from polished suspension, as labeled. In Figure 36(c) and (d), interface regions with two bonding areas were present, but the thickness of them were smaller than the interfaces present in Figure 34(b) and 29(b). It was possibly because higher sintering temperature provided more energy for atoms to

diffuse and formed better bonding areas. In addition, current defect paths were also found in this sample. They had the similar morphology as in Figure 35(c). However, the defects shown in Figure 36(c) and (d) were not as big and obvious as in Figure 35(c). It could be a result of better bonding situation, since the whole sample was more stable after higher temperature sintering.

Particularly, in Figure 36(b), current defects were found on the edge of this sample. Most of the current defects followed the direction as labeled in the image. Different from other current defects (see Figure 36(c) and (d)), in this image, the density of current defects was much higher and most of them followed the same direction. This indicated that the current density on the edge was higher than the rest of the sample. This morphology gave a confirmation for the modeling work done by Tamburini[17], which reported that the edge area of the conductive sample experienced higher current density during the SPS process.

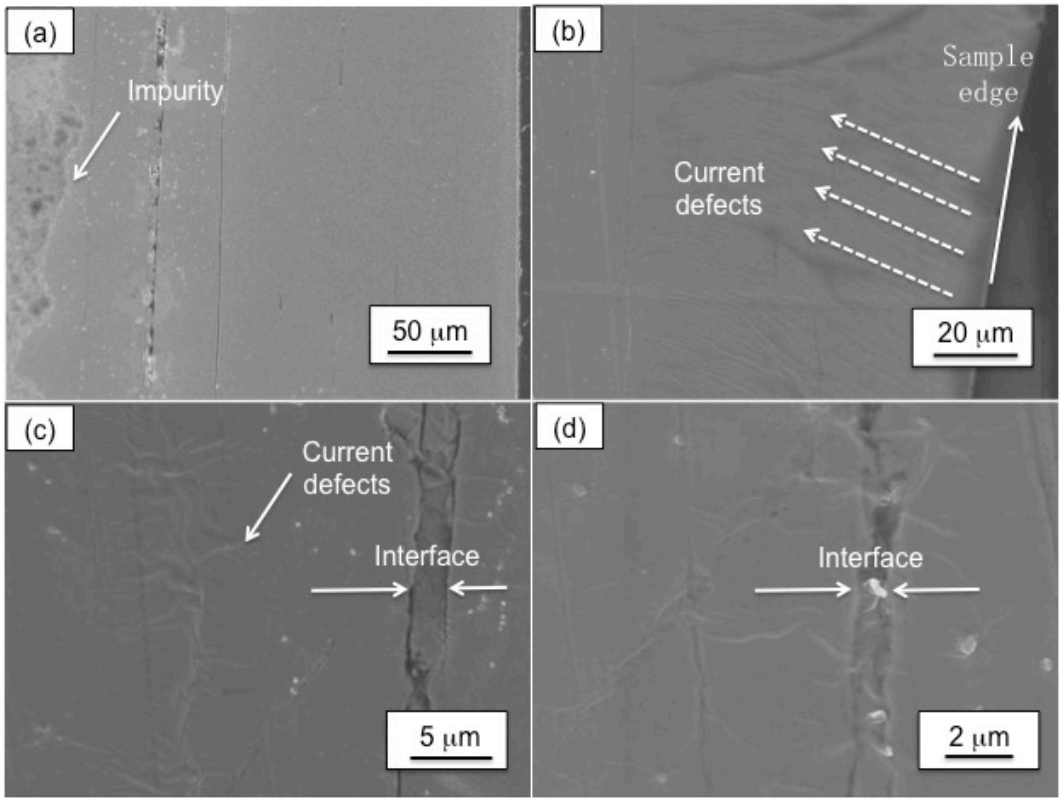

Figure 36: SEM images of Ni3 SPS samples sintered at T_x+30 K, and held for 20 min.

In Figure 37, a variety of SEM images of Ni3 samples, which was sintered in T_x+50 K by SPS, were shown with assorted regions and magnifications. From Figure 37(a), it could be seen that foils have more condense and solid bonds, as sintering temperature was higher. However, there were still several gaps where sintering did not ensue as vigorously, as shown in Figure 37(b). The gaps shown in Figure 37(b) were not continuous. In the center of the gap, foils were bonded solid, but the rest of the part remained independent. In Figure 37(c), an interface with unbonded area and current defects on the surface was shown. In addition, Figure 37(d) is the image of Figure 37(c) with higher magnification. Similar to the defects

observed in previous SPS samples (Figure 28, 26 and 28), the current defects had thunder-like morphology and lighter contrast under SEM. Those current defects had connected paths between two foils. It is believed that electric current could enhance the sintering process and crystallization kinetics.[12,14]

Also, Figure 37(e)-(h) showed two regions where current defects had one bright spot in the middle. The actual nature of this bright spot was hard to determine only by SEM. They have attracted attention due to their unique morphology. Every bright spot has been surrounded by a series of defects, spreading their paths into surrounding areas. However, based on the consideration that acetone and ultrasonication were used to remove the polished suspension residue, polished suspension could be excluded. The bright spots could be initial state of crystallization that had bright contrast under SEM. Under the assumption that the bright spot was the initial stage of crystallization, it could prove the theory that electric current had enhancement effect on crystallization kinetics by visual evidence.

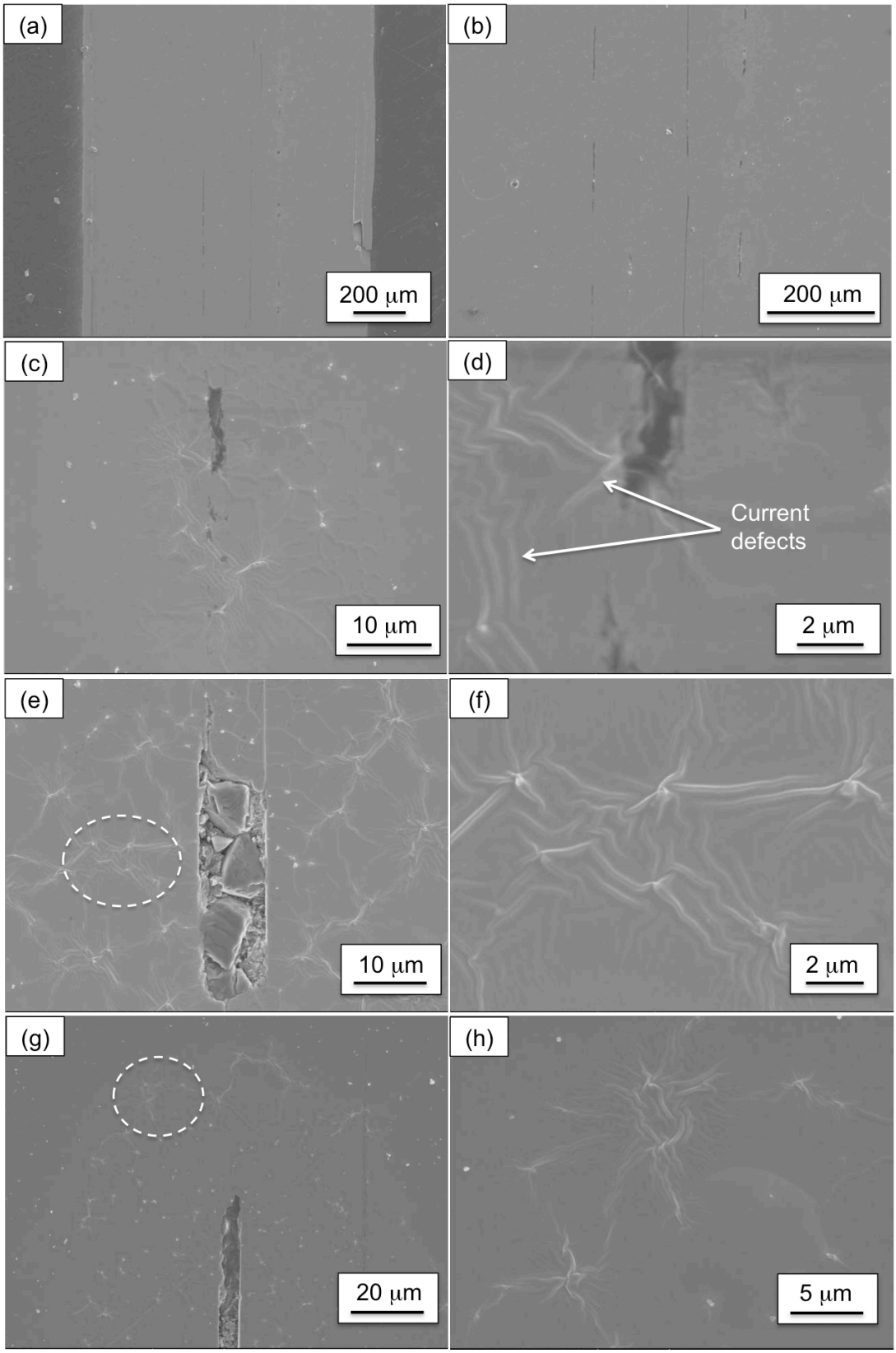

Figure 37: SEM images of Ni3 SPS samples sintered at T_x+50 K, and held for 20 min

As the sintering temperature increased, more condensed and

well-bonded samples were obtained because higher energy was supplied from sintering process. It was obvious in Figure 38(a) that the Ni3 sample was sintered almost fully by SPS at 873 K. Furthermore, according to its corresponding XRD pattern, this sample had sharp and intense XRD peaks, indicating that it was fully crystalline. It could be seen in Figure 38(a) that, on the left side near sample edge, there were several regions where foils were not fully bonded together. Figure 38(b) showed a closer look at that region. The thick interface, approximately 5μm, formed between two foils, was visible in Figure 38(b). A poor sintering and a strong diffusion process during the SPS were the most probable causes for the formation of this thick interface. In addition, no current defects, similar to those appearing in previous samples at lower sintering temperatures, were found in this sample. Compared with other Ni3 samples sintered at lower temperatures, the sample had fewer current defects as sintering temperature increases. This indicated that a flat and solid interface obtained in this Ni3 sample at 873 K had no current defect.

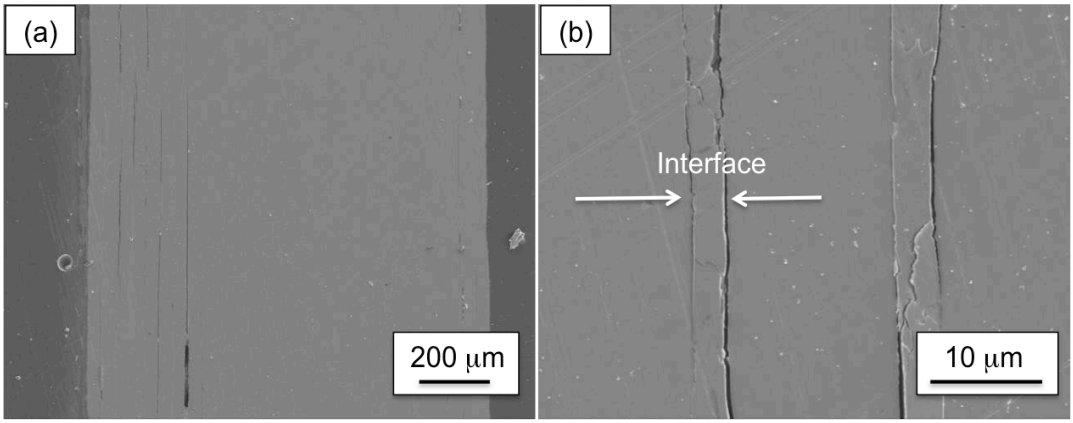

Figure 38: SEM images of Ni3 SPS samples sintered at 873 K (600°C), and held for 20 min.

As shown in Figure 39(a), Ni4 foils did not sinter creating strong and solid bond at T_x+10 K, due to the relatively low sintering temperature. In addition, surface microscopy showed that several foils broke in the middle. The possible reason for this, as mentioned in the previous discussion, might be the high pressure applied during the SPS or thermal shock at the end of the SPS. Images of the Ni4 sample in higher magnification were presented on Figure 39(b)-(d). Shown in Figure 39(c), there were a large number of thick interfaces exhibiting large thickness with crack in their interfaces. The typical thickness of the interface could reach several micrometers, as shown in Figure 39(c) and (d). In addition, between the interface and the Ni4 foil, small gaps filled with particles were seen. Those particles might be the product of diffusion and crystallization. However, those thick interfaces and their surrounding areas also presented the unique defects as observed in Ni2 and Ni3 samples. They had river-like defects, which could be caused by two reasons. The first was the electric current-induced diffusion, since high

intensity of electric current has been applied in SPS. This high concentration of electric current was believed to enhance the bonding process and crystallization reaction by a variety of researchers.[7,8,11,12,18,60] The second reason was the thermal shock as was mentioned earlier at Ni3 sample's (Figure 34) discussion. Taking into consideration that samples have been left in air after heating process, a significant cooling process happened throughout the sample，which might have caused cracks and some changes in morphology, as the interface areas were fragile and not as robust as the foils.

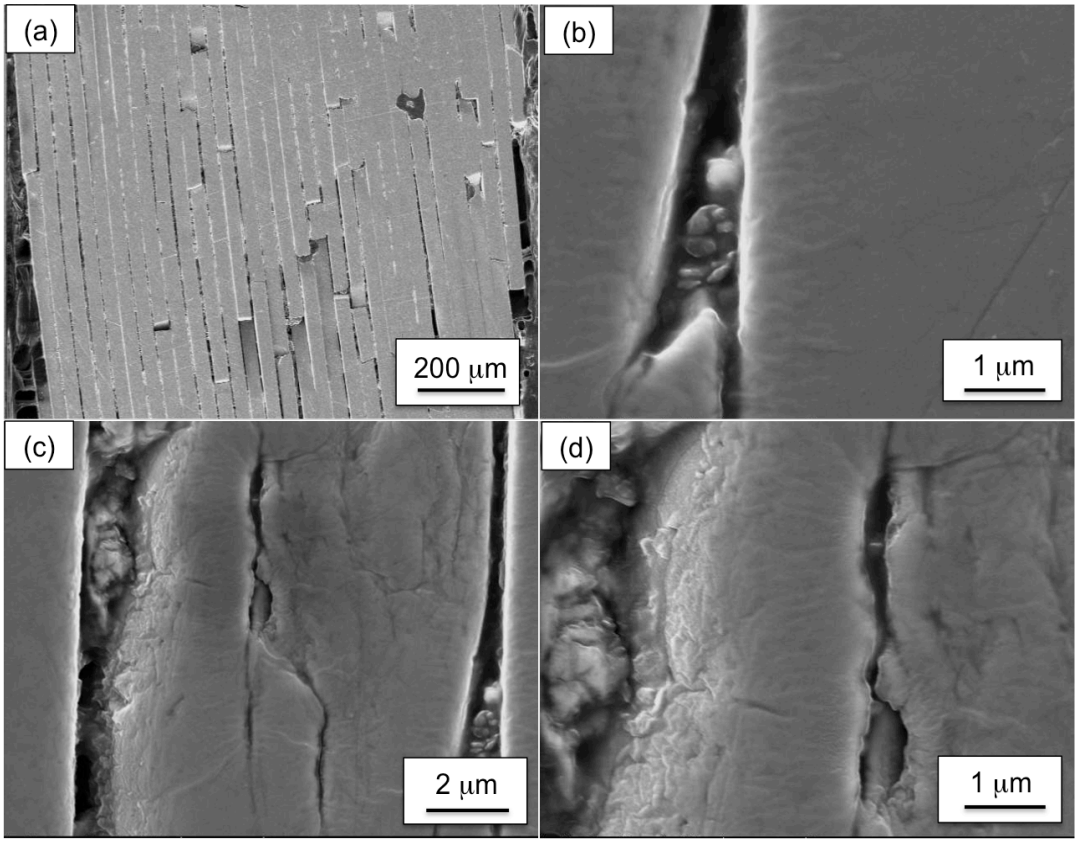

Figure 39: SEM images of Ni4 SPS sample sintered at T_x+10 K, and held for 20 min.

In Figure 40, Ni4 foils SPS sample, which was sintered at T_x+20 K, was

shown. As shown in Figure 40(a), the foils were fairly sintered together. The extent of sintering altered from region to region, similar to the Ni4 sample in Figure 39. Compared to Ni4 sample sintered at T_x+10 K (Figure 39), where sample was sintered weakly, this samples showed a slight improvement of consolidation. A really weak bonding between foils was shown in Figure 40(a). Some of the bonds even lack a continuous morphology. In Figure 40(b), the interface labeled was filled with fragments of materials. These fragmented interfaces might be the result of initial diffusion and/or fast cooling process. In Figure 40(c) and (d), a region with bright spots was observed. In a higher magnification (Figure 40(d)), it was observed that every bright spot was surrounded by several defect-paths in different directions. Basically, it seemed like the defects stemmed from the center of bright spot. EDX was also performed on this specific area, as shown in Figure 41. In Figure 41(c), a small oxygen signal was detected, indicating that little oxidation happened on the surfaces. Iridium signals came from the iridium sputtering coating for conductive surfaces under SEM. Besides Ni, Cr and Si, which were the composition of this kind of alloy, C was also detected according to the results. Elemental mapping with Si and C was shown with corresponding element label in Figure 41(b). The red spots, representing carbon, distributed homogeneously throughout the area. However, the green spots, corresponding to Si, had a higher density,

especially close to the interface areas. This indicated that those bright spots were not from polish process. They might have a close relationship to enhanced movement of Si atoms during the SPS process. Considering the fact that those spots positioned in the center of defects, they could also relate to the formation of the defects surrounding them. However, further confirmation tests needed to be done in the future to verify the formation mechanism of those bright spots and defects, including detailed TEM analysis.

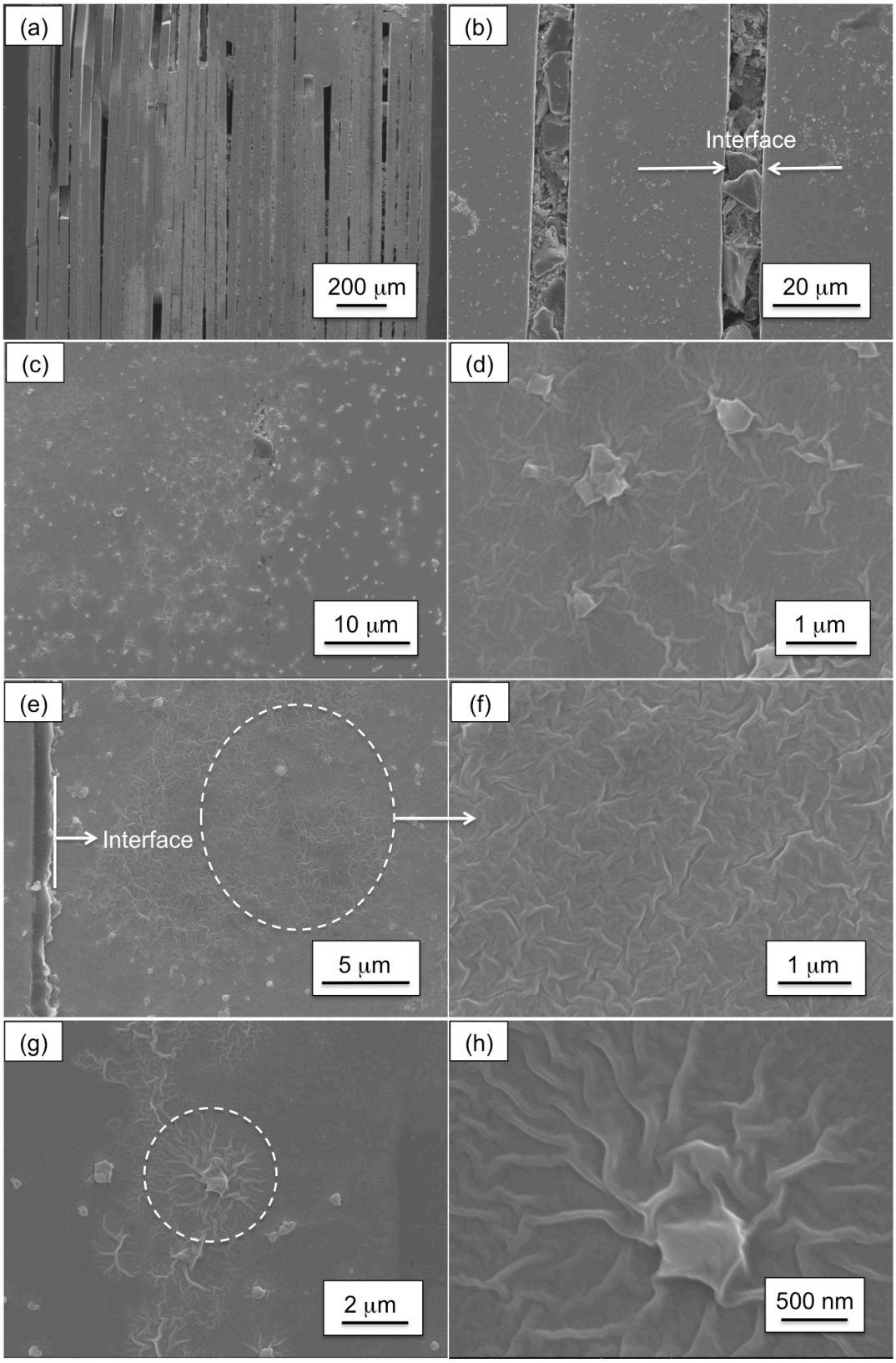

Figure 40: SEM images of Ni4 SPS sample sintered at T_x+20 K, and held for 20 min.

In Figure 40(e) and (f), a region of high density of defects was shown.

As shown in Figure 40(e), this region was located next to the interface, and also exhibited bright spots. Compared to Figure 40(c), the density of bright spots in Figure 40(e) was smaller. The bright spots located on the edge of defects region. Figure 40(f) was a closer look of the defect region shown in Figure 40(e). As shown in Figure 40(f), the defects had a similar morphology as previous regions. This area was also checked using EDX, as shown in Figure 42, and no evidence of significant oxidation or residues from the sample preparation was found. In addition, the size of the defects, which was approximately several hundreds of nanometers (see Figure 40(f) and (h)), excluded the possibility that they were the grain boundaries of crystalline materials. Those reasons indicated that the morphology of bright spots and surrounded defects would be a result from sintering process. In Figure 40(g) and (h), another region with similar pattern of defects is shown with two magnifications. The defects patterns shown in Figure 40(g) and (h) positioned along the interface direction, which was similar as Ni2 SPS samples (see Figure 34). Since there was no related morphology reported before, these defects might have a close relationship to applied electric current during the SPS process.

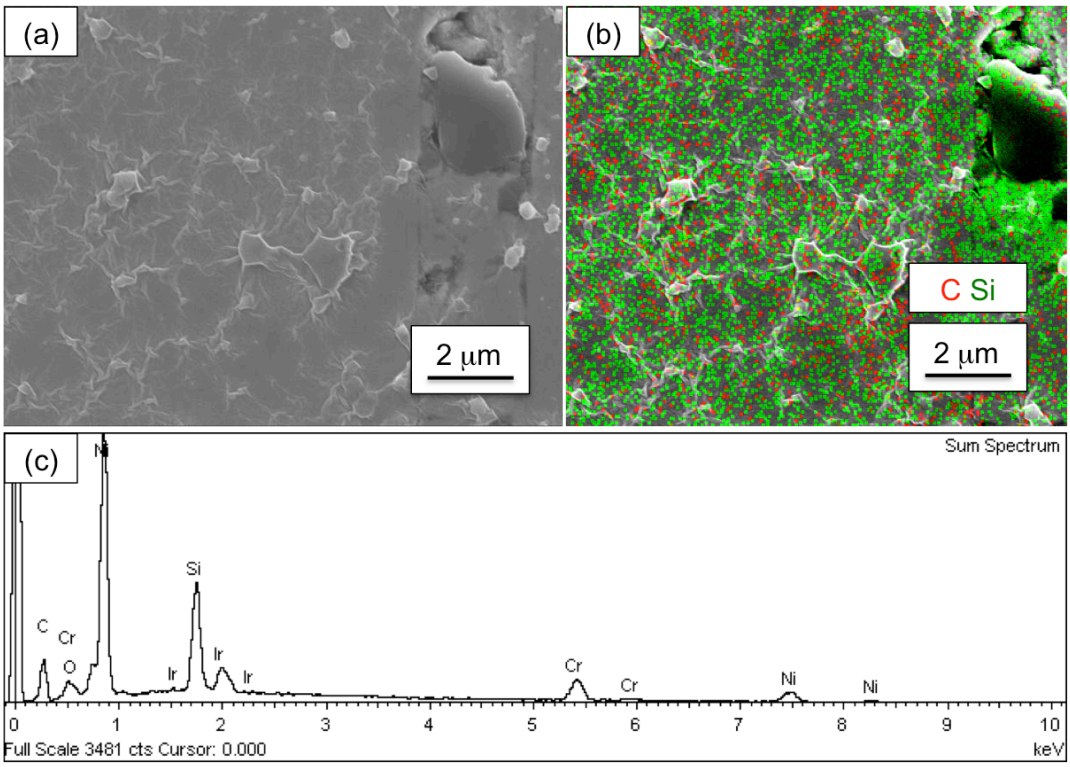

Figure 41: Ni4 SPS sample sintered at T_x+20 K, and held for 20 min: (a) SEM image; (b) corresponding EDX mapping; (c) and corresponding EDX spectrum.

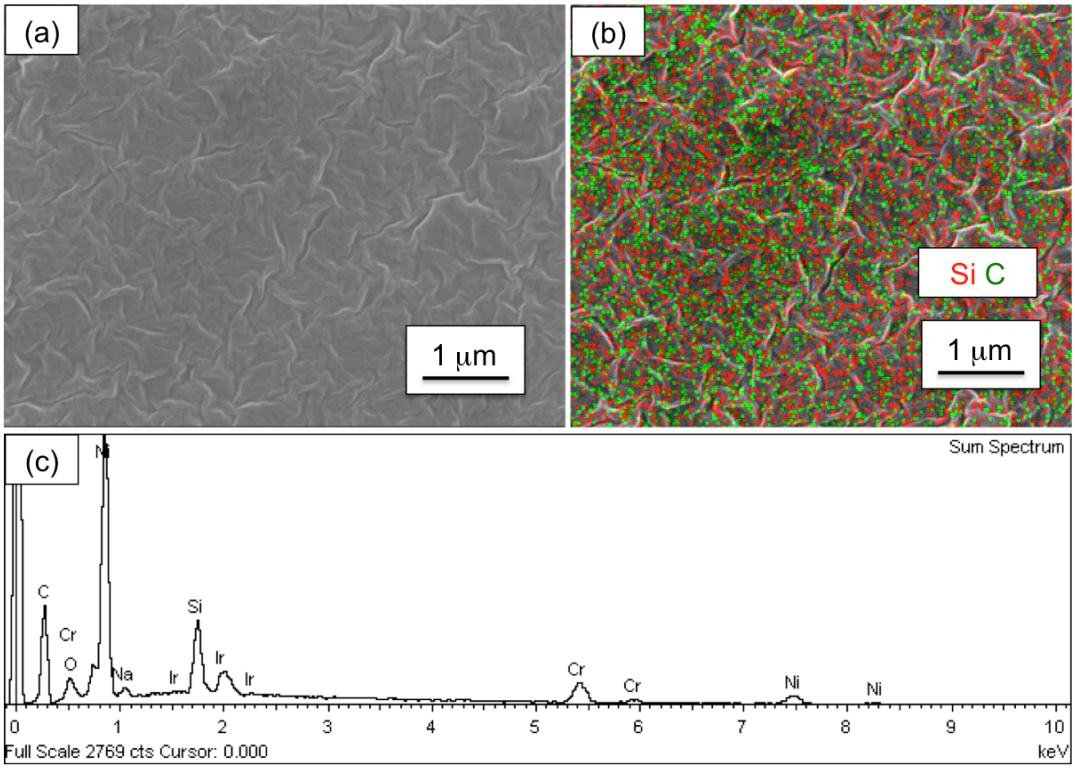

Figure 42: Ni4 SPS sample sintered at T_x+20 K, and held for 20 min: (a) SEM image; (b) corresponding EDX mapping; (c) and corresponding EDX spectrum.

As shown in the Figure 43(a), Ni4 foils sintered at T_x+30 K, exhibited better bonding strength. The sample surface seemed more condensed, and there were less gaps and cleavages present in the surface. Since higher sintering temperature could provide more energy for materials to diffuse and bond, Ni4 foils sintered at T_x+30 K should have better sintering behavior than in lower temperatures (T_x+10 K and T_x+20 K). In Figure 43(b), it could be seen that the thick interface was undergoing a closing process, bonding two foils together, as the sintering temperature raised higher. In some areas of the interface, solid and flat bonding was obtained. Figure 43(c) was a zoomed-in image of Figure 43(b), since there was much unique surface

morphology presented. There were a variety of bright spots sitting in the surface shown in Figure 43(c), and some of them were on the path of current defects. The pattern of these current defects shown in Figure 43(c) was different from samples sintered at T_x+10 K and T_x+20 K (see Figure 39 and 34).

In Figure 43(e)-(g), another region of interface with significant current defects are presented. Figure 43(g) and (f) are the images with higher magnifications. The common feature of current defects in Figure 43(e)-(g) was that they have one bright point in the middle of the defects path. This kind of current pattern has been observed in Figure 40, where the sample was sintered at T_x+20 K. Considering that these three samples sintered at different temperatures exhibited different current defect patterns, it might experience a transformation process of current defect morphologies. However, the deep understanding of these defects and the mechanism of this morphology transformation were still unknown.

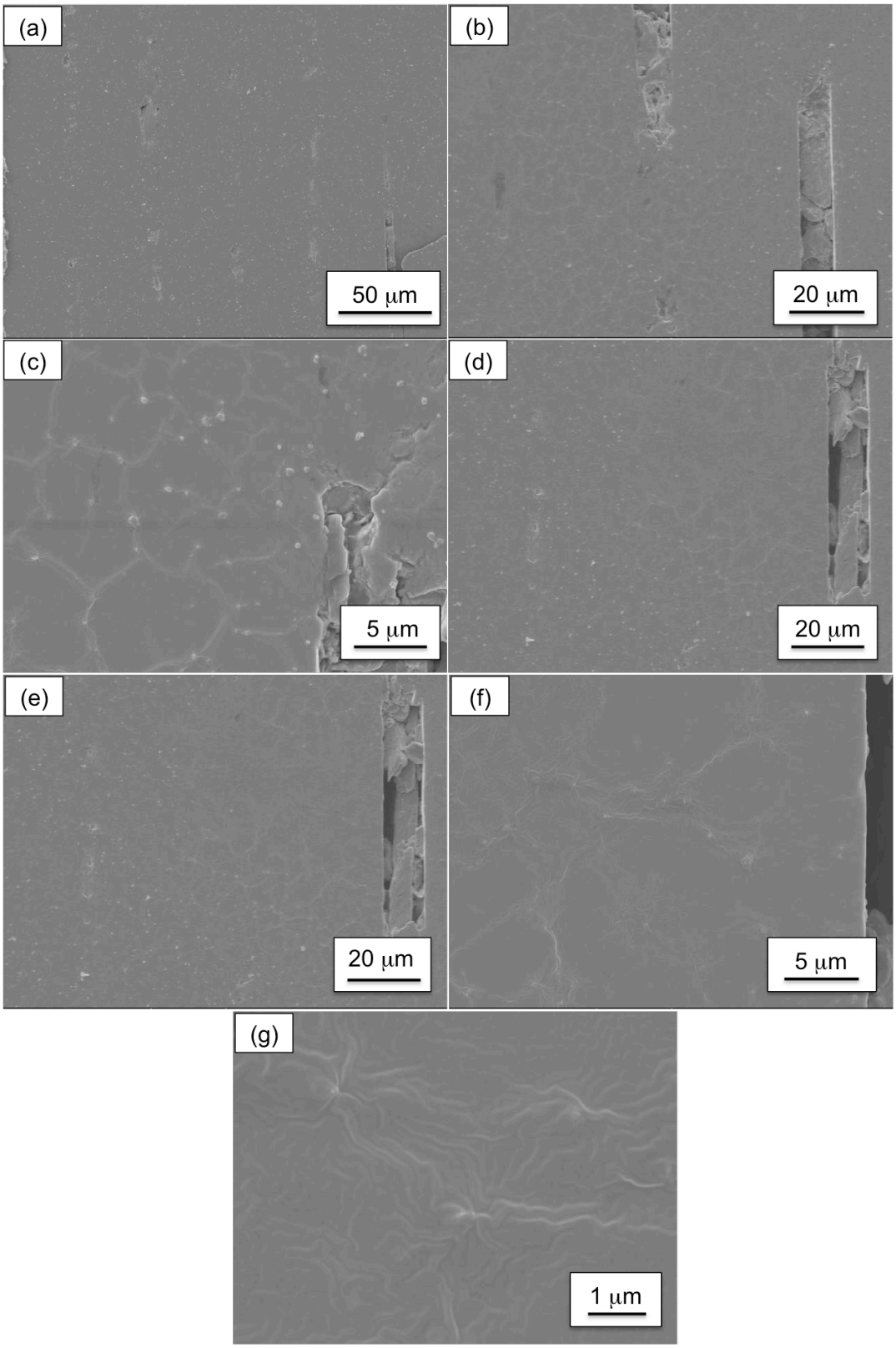

Figure 43: SEM images of Ni4 SPS sample sintered at T_x+30 K, and held for 20 min.

In Figure 44, Ni4 foils sintered at T_x+50 K are shown in a variety of

magnifications. As shown in Figure 44(a), foils were sintered better due to the higher sintering temperature. In this sample, there were still thick interfaces, several micrometers thick, shown in Figure 44(b) and (g). However, the interface was generally solid throughout the perpendicular direction and had narrow and flat bonding areas with neighboring foils. These were all a result from the higher sintering temperature. Similar as previous Ni4 samples sintered at lower temperatures, current defects were observed on the surface. In general, the current defect paths shown in Figure 44(c) and (d) had a loop pattern, which was similar as Figure 43(g). In addition, these current defects were condensed, wide, and had a brighter contrast. Specifically, in Figure 44(d), the current defect paths spread out into different directions from one center, which was similar as in Figure 40(h). However, in comparison to current defects shown in Figure 40(h), the current defects in Figure 44(b) and (g) did not have large bright spots in the center.

In Figure 44(e) and (f), another interface region with current defects was shown. Different from interface shown in Figure 44(b), which exhibited two bonding interfaces, the interface shown in Figure 44(e) had only one bonding interface. Figure 44(g) and (h) showed an interface with current defects and crack on it. The crack was labeled in the image. Due to the smooth edge and continuous shape of this crack, the crack could be the result of pre-existing strain in the original foils. During the high-temperature sintering,

the edge of this crack has been smoothened under diffusion.

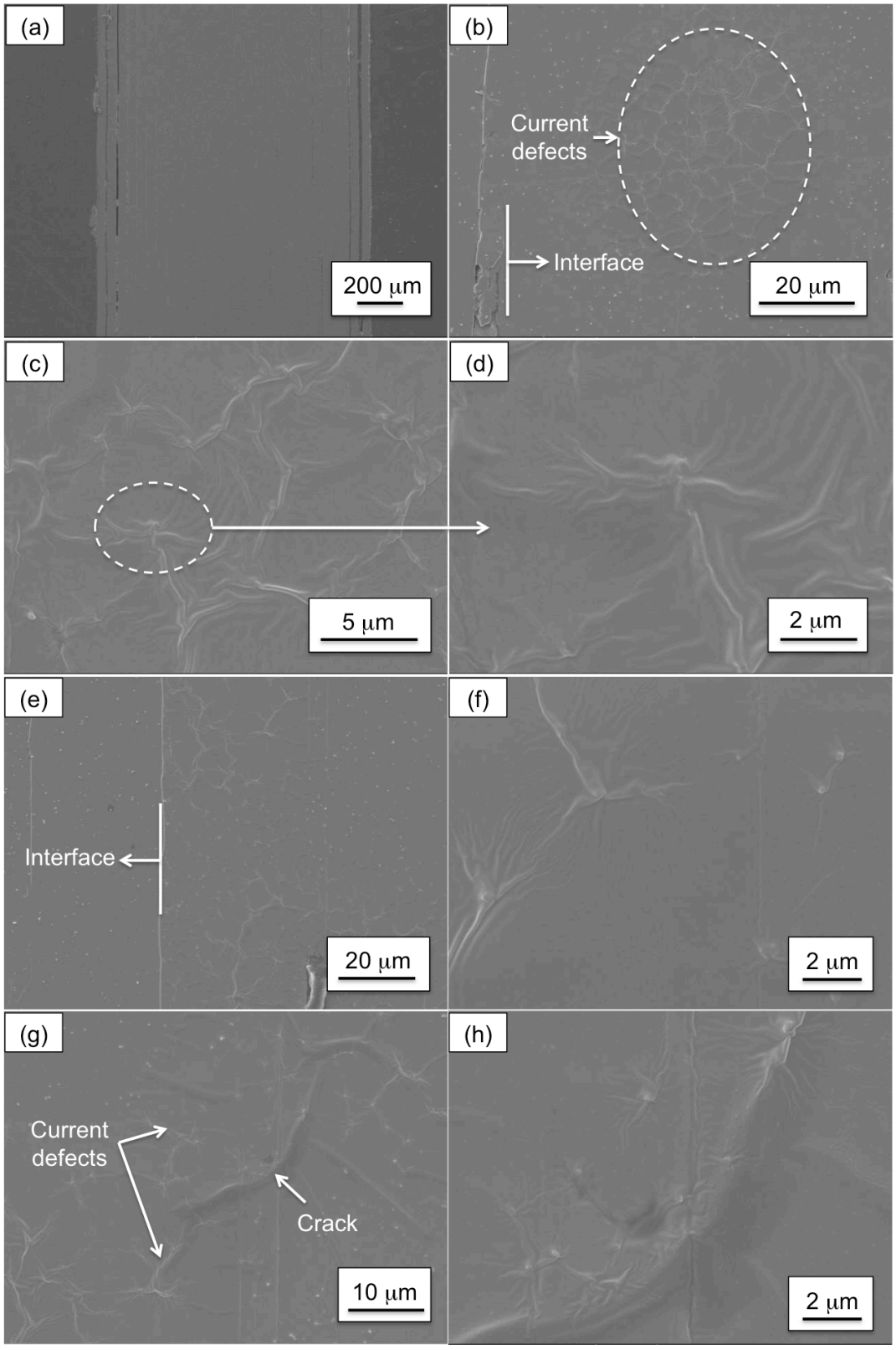

Figure 44: SEM images of Ni4 SPS sample sintered at T_x+50 K, and held for 20 min.

In Figure 45, images of Ni4 foils sintered at 873 K were shown with a variety of magnifications. From Figure 45(a) and (d), it could be seen that this sample has been sintered to a highly condensed state with a strong bonding between each foil. Most of the foils in this sample exhibited interface morphologies similar to those shown in Figure 45(d), where foils were bonded with only one interface. This phenomenon indicated a better sintering result and stronger bonding situation at the highest sintering temperature. In Figure 45(b), an interface with approximately 5μm had been formed possibly due to a diffusion process at this sintering temperature. Compared to the interfaces with comparable thickness in previous samples (see Figure 39(c), Figure 40(b), Figure 43(b) and Figure 44(b)), the interfaces shown in Figure 45(b) were more condensed and had flatter bonding areas with surrounding foils. In general, there was no obvious gaps or pores present in Figure 45(b). However, there was a crack as labeled in Figure 45(b). Moreover, the interface was a relatively weak area, with two bonding interfaces formed during SPS. High cooling rate after SPS might have induced a thermal shock effect to create a micro-size crack inside the interface. In addition, since the direction of this crack was perpendicular to the foils' direction, this crack should be caused by thermal shock occurring during the cooling process of SPS. Besides cracks, there were some bright spots presenting in the surface of samples. The possible reason for these

spots was unknown only according to SEM characterization. Further exploration is needed to study the details.

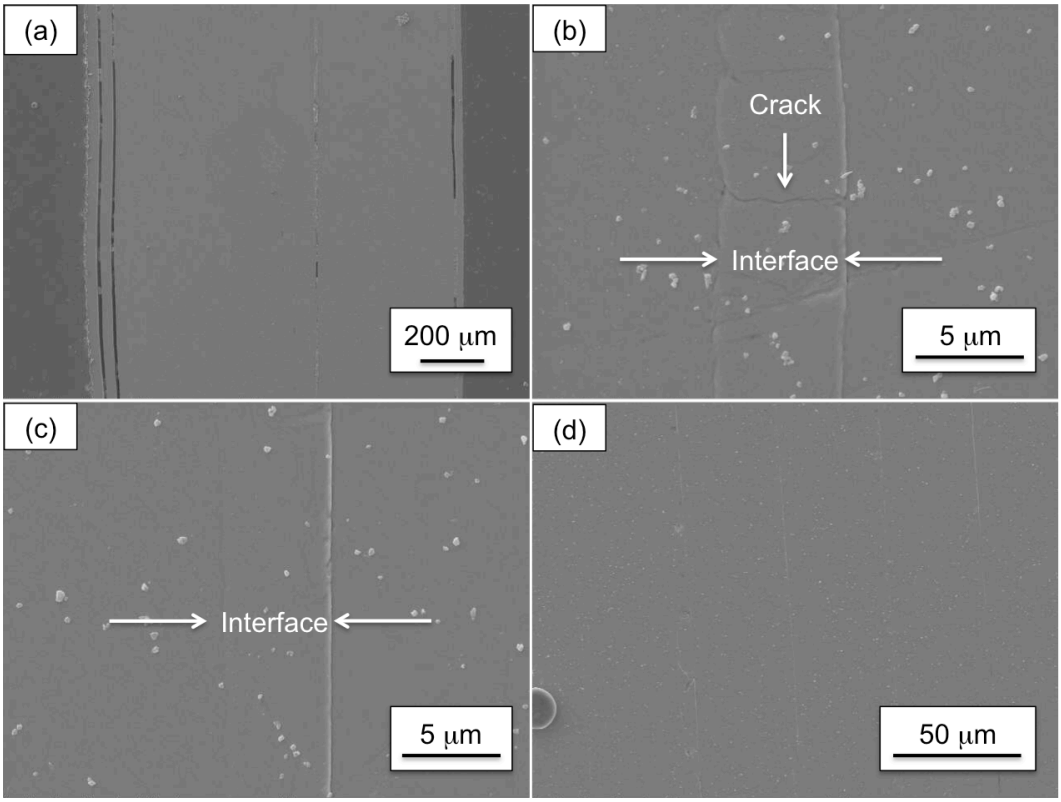

Figure 45: SEM images of Ni4 SPS sample sintered at 873 K (600°C), and held for 20 min.

4 Summary

Four different Ni-based amorphous alloy foils were sintered at different temperatures. Both SPS and pressureless sintering were used to compare the sintering behavior of each material, including thermodynamic behavior, XRD patterns and cross-section morphology. Different alloy compositions exhibit different DSC curves, which means alloy composition has an effect on material thermodynamic properties. As presented in Table 2, all five Ni-based amorphous metal foils present multiple exothermic reaction stages within the same heating range. However, the exothermic reaction temperatures (heat flow peaks) and the number of reactions vary from alloy to alloy. With a series of heating rates tested, Kissinger theory was used to calculate the activation energy of each material under isothermal process. As shown in Figure 15, all of the data points fit linear perfectly. This multiple exothermic reaction phenomenon is believed to have a close relationship to the multiple devitrification stages of these alloys.

To solidify this assumption, XRD was performed for every sintered sample, including SPS and pressureless sintering samples. According to a detailed XRD analysis, and full-width-half-maximum (FWHM) measurements, those alloys showed different devitrification kinetics under SPS and free sintering. At a relatively low temperature, samples from free sintering

present a higher crystallinity due to a longer holding time. However, as temperature increases, FWHM for SPS samples dropped significantly and reached a comparable value as pressureless sintering samples. These results indicate that SPS samples experienced faster crystallization kinetics compared to pressureless sintering. The faster kinetics may be contributed by lower activation energy required for crystallization as electric current applied in the SPS[8]. In addition, XRD phase identification also indicates that relatively low temperature SPS will result in metastable phase formation in materials, as discussed in Chapter 3.2. As sintering temperature increases, the metastable phases would be replaced by stable phases, which are the same as in free sintering. Specifically, as shown in Figure 16(a), 18(a), 19(a) and 20(a), Ni-Cr compounds were formed at relatively low temperatures, which were around T_x+10 K and T_x+20 K. However, the pressureless sintering samples at the same sintering temperatures exhibited Ni-Si compounds. As sintering temperature increased, Ni-Cr compounds transformed to Ni-Si, which were the same compounds obtained from free sintering.

To explore the microstructure of each sample, cross section morphologies were observed carefully using SEM analysis. A unique morphology has been found in SPS samples. Due to a severe diffusion process, which happened during sintering, thick interfaces, several

micrometers thickness, have been formed. As shown in Figure 28, Figure 32, 28, 31, 34, 37 and 38, current defects near interface exhibited similar morphology. They had several current defect paths spreading into different directions from the center of them. In addition, the contrast of those current defects was brighter than the surrounding areas. In addition, in the center of the current defect paths, there was one bright spot. Especially in Figure 40(g), the size of bright spot was big, approximately 400nm diameter, and the amount of these bright spot was large. However, as sintering temperature increased, as shown in Figure 43(g), and Figure 44(d)-(g), the bright spots experienced a transformation period, which gradually minimized and became less bright as in Figure 43(g). Compared to the overall experimental temperatures, samples sintered at lower temperature tend to have more defects around the interface, due to a poor bonding condition. Furthermore, the thickness of interface region also exhibits a trend as different experimental temperatures were used. At relatively low temperature, as in Figure 28(a), 28(b), and 33(c), the thickness of those interface regions were ~5 μm, and there are two bonding interfaces presented. When temperature increases to the highest value, 873 K, interface regions presented in Figure 38 and 39 showed only one bonding interface, or thinner interface regions. This indicates that, as sintering temperature increases, a more solid sample and better bonding are obtained, so there are fewer defects and interface

regions become thinner. It could be concluded that those current defects have a positive effect on foil bonding process. It is possible that those defects have a close relationship to electric current since current is proved to enhance the sintering behavior during SPS.[7,8,11,16,18,60] In addition, pressure is also another possible reason, as high uniaxial pressure was applied during the SPS, and previous research has reported the enhancement due to pressure.[58,63] However, since a deep understanding of current defect formation mechanism and further characterization focused on those defects are still lacking, more exploration on this unique morphology is still required in the near future.

5 Reference

1 Kingery, W. D. in *Trans Tech* Vol. p.1 (ed J.A. Lund A.C.D. Chaklader) (Brookfiled, 1992).

2 Hulbert, D. M., Anders, A., Andersson, J., Lavernia, E. J. & Mukherjee, A. K. A discussion on the absence of plasma in spark plasma sintering. *Scripta Materialia* **60**, 835-838 (2009).

3 Munir, Z. A., Quach, D. V. & Ohyanagi, M. Electric current activation of sintering: a review of the pulsed electric current sintering process. *Journal of the American Ceramic Society* **94**, 1-19 (2011).

4 Hulbert, D. M., Jiang, D., Dudina, D. V. & Mukherjee, A. K. The synthesis and consolidation of hard materials by spark plasma sintering. *International Journal of Refractory Metals and Hard Materials* **27**, 367-375 (2009).

5 Nishimura, T., Mitomo, M., Hirotsuru, H. & Kawahara, M. Fabrication of silicon nitride nano-ceramics by spark plasma sintering. *Journal of materials science letters* **14**, 1046-1047 (1995).

6 Gu, Y., Khor, K. & Cheang, P. Bone-like apatite layer formation on hydroxyapatite prepared by spark plasma sintering (SPS). *Biomaterials* **25**, 4127-4134 (2004).

7 Anselmi-Tamburini, U., Garay, J. & Munir, Z. Fundamental investigations on the spark plasma sintering/synthesis process: III. Current effect on reactivity. *Materials Science and Engineering: A* **407**, 24-30 (2005).

8 Bertolino, N., Garay, J., Anselmi-Tamburini, U. & Munir, Z. Electromigration effects in Al-Au multilayers. *Scripta materialia* **44**, 737-742 (2001).

9 Chen, W., Anselmi-Tamburini, U., Garay, J., Groza, J. & Munir, Z. A. Fundamental investigations on the spark plasma sintering/synthesis process: I. Effect of dc pulsing on reactivity. *Materials Science and Engineering: A* **394**, 132-138 (2005).

10 Frei, J. M., Anselmi-Tamburini, U. & Munir, Z. A. Current effects on

neck growth in the sintering of copper spheres to copper plates by the pulsed electric current method. *Journal of applied physics* **101**, 114914 (2007).

11 Friedman, J., Garay, J., Anselmi-Tamburini, U. & Munir, Z. A. Modified interfacial reactions in Ag–Zn multilayers under the influence of high DC currents. *Intermetallics* **12**, 589-597 (2004).

12 Garay, J., Anselmi-Tamburini, U. & Munir, Z. A. Enhanced growth of intermetallic phases in the Ni–Ti system by current effects. *Acta Materialia* **51**, 4487-4495 (2003).

13 Garay, J. E., Glade, S. C., Anselmi-Tamburini, U., Asoka-Kumar, P. & Munir, Z. A. Electric current enhanced defect mobility in Ni 3 Ti intermetallics. *Applied Physics Letters* **85**, 573-575 (2004).

14 Liao, C.-N. & Wu, L.-C. Enhancement of carrier transport properties of BixSb2-xTe3 compounds by electrical sintering process. *Applied Physics Letters* **95**, 2112 (2009).

15 Toyofuku, N., Kuramoto, T., Imai, T., Ohyanagi, M. & Munir, Z. A. Effect of pulsed DC current on neck growth between tungsten wires and tungsten plates during the initial stage of sintering by the spark plasma sintering method. *Journal of Materials Science* **47**, 2201-2205 (2012).

16 Zhuang, Y. X., Yi, S. S. & Wang, W. H. Electric-field-enhanced crystallization of Zr41Ti14Cu12.5Ni10Be22.5 bulk metallic glass. *Materials Transactions* **42**, 583-586, doi:10.2320/matertrans.42.583 (2001).

17 Anselmi-Tamburini, U., Gennari, S., Garay, J. & Munir, Z. A. Fundamental investigations on the spark plasma sintering/synthesis process: II. Modeling of current and temperature distributions. *Materials Science and Engineering: A* **394**, 139-148 (2005).

18 Zhao, J., Garay, J. E., Anselmi-Tamburini, U. & Munir, Z. A. Directional electromigration-enhanced interdiffususion in the Cu–Ni system. *Journal of Applied Physics* **102**, 114902 (2007).

19 Tokita, M. in *Proceeding of NEDO International Symposium on Functionally Graded Materials.* 22 (Japan).

20 Castro, R. & van Benthem, K. *Sintering: mechanisms of convention nanodensification and field assisted processes*. Vol. 35 (Springer Science & Business Media, 2012).

21 Smirnov, B. M. *Plasma Processes and Plasma Kinetics: 580 Worked-Out Problems for Science and Technology*. (John Wiley & Sons, 2008).

22 Anders, A. *Cathodic arcs: from fractal spots to energetic condensation*. Vol. 50 (Springer Science & Business Media, 2009).

23 Chapman, B. *Glow discharge processes: sputtering and plasma etching*. (Wiley-Interscience, 1980).

24 Ho, P. S. & Kwok, T. Electromigration in metals. *Reports on Progress in Physics* **52**, 301 (1989).

25 Tu, K. Electromigration in stressed thin films. *Physical Review B* **45**, 1409 (1992).

26 Hsu, C.-M., Wong, D. S.-H. & Chen, S.-W. Generalized phenomenological model for the effect of electromigration on interfacial reaction. *Journal of Applied Physics* **102**, 023715 (2007).

27 Techaumant, B. & Takuma, T. Calculation of electric field and force on conductor particles with a surface film. *Magnetics, IEEE Transactions on* **41**, 1388-1391 (2005).

28 Klement, W., Willens, R. H. & Duwez, P. NON-CRYSTALLINE STRUCTURE IN SOLIDIFIED GOLD-SILICON ALLOYS. *Nature* **187**, 869-870, doi:10.1038/187869b0 (1960).

29 Cohen, M. H. & Turnbull, D. Molecular transport in liquids and glasses. *The Journal of Chemical Physics* **31**, 1164-1169 (1959).

30 Inoue, A. & Takeuchi, A. Recent progress in bulk glassy alloys. *Materials Transactions* **43**, 1892-1906, doi:10.2320/matertrans.43.1892 (2002).

31 Chen, H.-s. & Polk, D. (Google Patents, 1974).

32 Inoue, A., Zhang, T., Nishiyama, N., Ohba, K. & Masumoto, T. PREPARATION OF 16 MM DIAMETER ROD OF AMORPHOUS

ZR65AL7.5NI10CU17.5 ALLOY. *Materials Transactions Jim* **34**, 1234-1237 (1993).

33 Inoue, A. Stabilization of metallic supercooled liquid and bulk amorphous alloys. *Acta Materialia* **48**, 279-306, doi:10.1016/s1359-6454(99)00300-6 (2000).

34 Peker, A. & Johnson, W. L. A HIGHLY PROCESSABLE METALLIC-GLASS - ZR41.2TI13.8CU12.5NI10.0BE22.5. *Applied Physics Letters* **63**, 2342-2344, doi:10.1063/1.110520 (1993).

35 Wang, W. H., Dong, C. & Shek, C. H. Bulk metallic glasses. *Materials Science & Engineering R-Reports* **44**, 45-89, doi:10.1016/j.mser.2004.03.001 (2004).

36 Inoue, A. & Takeuchi, A. Recent progress in bulk glassy, nanoquasicrystalline and nanocrystalline alloys. *Materials Science and Engineering: A* **375**, 16-30 (2004).

37 Flores, K. M. & Dauskardt, R. H. Local heating associated with crack tip plasticity in Zr–Ti–Ni–Cu–Be bulk amorphous metals. *Journal of materials research* **14**, 638-643 (1999).

38 Flores, K. M. & Dauskardt, R. H. Enhanced toughness due to stable crack tip damage zones in bulk metallic glass. *scripta materialia* **41**, 937-943 (1999).

39 Gilbert, C., Ritchie, R. & Johnson, W. Fracture toughness and fatigue-crack propagation in a Zr–Ti–Ni–Cu–Be bulk metallic glass. *Applied Physics Letters* **71**, 476-478 (1997).

40 Bruck, H., Christman, T., Rosakis, A. & Johnson, W. Quasi-static constitutive behavior of Zr 41.25 Ti 13.75 Ni 10 Cu 12.5 Be 22.5 bulk amorphous alloys. *Scripta Metallurgica et Materialia* **30**, 429-434 (1994).

41 Flores, K. M., Johnson, W. L. & Dauskardt, R. H. Fracture and fatigue behavior of a Zr–Ti–Nb ductile phase reinforced bulk metallic glass matrix composite. *Scripta materialia* **49**, 1181-1187 (2003).

42 Hays, C. C. *et al.* Vitrification and determination of the crystallization time scales of the bulk-metallic-glass-forming liquid Zr58.5Nb2.8Cu15.6Ni12.8Al10.3. *Applied Physics Letters* **79**,

1605-1607, doi:10.1063/1.1398605 (2001).

43 Bruck, H. A., Rosakis, A. J. & Johnson, W. L. The dynamic compressive behavior of beryllium bearing bulk metallic glasses. *Journal of Materials Research* **11**, 503-511 (1996).

44 Conner, R., Dandliker, R. & Johnson, W. L. Mechanical properties of tungsten and steel fiber reinforced Zr 41.25 Ti 13.75 Cu 12.5 Ni 10 Be 22.5 metallic glass matrix composites. *Acta Materialia* **46**, 6089-6102 (1998).

45 Schuh, C., Hufnagel, T. & Ramamurty, U. Mechanical behavior of amorphous alloys. *Acta Materialia* **55**, 4067-4109, doi:10.1016/j.actamat.2007.01.052 (2007).

46 He, Y., Price, C., Poon, S. & Shiflet, G. Formation of bulk metallic glasses in neodymium-based alloys. *Philosophical magazine letters* **70**, 371-377 (1994).

47 Xing, L. Q., Eckert, J., Löser, W., Roth, S. & Schultz, L. Atomic ordering and magnetic properties in Nd57Fe20B8Co5Al10 solids. *Journal of Applied Physics* **88**, 3565-3569 (2000).

48 Wei, B. *et al.* Anomalous thermal stability of Nd–Fe–Co–Al bulk metallic glass. *Acta materialia* **50**, 4357-4367 (2002).

49 Michael E., M., Matthew A. Willard, David E. Luaghlin. Amorphous application as soft megnetics. *Progress in Materials Science* **44**, 291 (1999).

50 Shen, B., Akiba, M. & Inoue, A. Effects of Si and Mo additions on glass-forming in FeGaPCB bulk glassy alloys with high saturation magnetization. *Physical Review B* **73**, 104204 (2006).

51 Suryanarayana, C. & Inoue, A. Iron-based bulk metallic glasses. *International Materials Reviews* **58**, 131-166, doi:10.1179/1743280412y.0000000007 (2013).

52 Schroers, J., Busch, R., Bossuyt, S. & Johnson, W. L. Crystallization behavior of the bulk metallic glass forming Zr41Ti14Cu12Ni10Be23 liquid. *Materials Science and Engineering a-Structural Materials Properties Microstructure and Processing* **304**, 287-291, doi:10.1016/s0921-5093(00)01454-4 (2001).

53 Schroers, J., Busch, R. & Johnson, W. L. in *Metastable, Mechanically Alloyed and Nanocrystalline Materials, Pts 1 and 2* Vol. 343-3 *Materials Science Forum* (eds J. Eckert, H. Schlorb, & L. Schultz) 167-172 (2000).

54 Schroers, J., Busch, R., Masuhr, A. & Johnson, W. L. Nucleation in undercooled Zr41Ti14Cu12Ni10Be23 melts. *Journal of Non-Crystalline Solids* **250**, 699-703, doi:10.1016/s0022-3093(99)00163-5 (1999).

55 Schroers, J. & Johnson, W. L. Crystallization of Zr(41)Ti(14)Cu(12)Ni(10)Be(23). *Materials Transactions Jim* **41**, 1530-1537 (2000).

56 Schroers, J. & Johnson, W. L. History dependent crystallization of Zr41Ti14Cu12Ni10Be23 melts. *Journal of Applied Physics* **88**, 44-48, doi:10.1063/1.373621 (2000).

57 Wang, W. H., He, D., Zhao, D., Yao, Y. & He, M. Nanocrystallization of ZrTiCuNiBeC bulk metallic glass under high pressure. *Applied physics letters* **75**, 2770-2772 (1999).

58 Zhang, J. *et al.* Crystallization kinetics and pressure effect on crystallization of Zr55Al10Ni5Cu30 bulk metallic glass. *Materials Science and Engineering a-Structural Materials Properties Microstructure and Processing* **357**, 386-391, doi:10.1016/s0921-5093(03)00255-7 (2003).

59 Eckert, J., Mattern, N., Zinkevitch, M. & Seidel, M. Crystallization behavior and phase formation in Zr-Al-Cu-Ni metallic glass containing oxygen. *Materials Transactions Jim* **39**, 623-632 (1998).

60 Holland, T. B., Löffler, J. F. & Munir, Z. A. Crystallization of metallic glasses under the influence of high density dc currents. *Journal of applied physics* **95**, 2896-2899 (2004).

61 Dos Santos, D. & Dos Santos, D. Crystallization kinetics of Fe–B–Si metallic glasses. *Journal of non-crystalline solids* **304**, 56-63 (2002).

62 Kissinger, H. E. Reaction kinetics in differential thermal analysis. *Analytical chemistry* **29**, 1702-1706 (1957).

63 Munir, Z., Anselmi-Tamburini, U. & Ohyanagi, M. The effect of electric

field and pressure on the synthesis and consolidation of materials: a review of the spark plasma sintering method. *Journal of Materials Science* **41**, 763-777 (2006).